GEOPHYSICAL MEASUREMENTS OF BASALT INTRAFLOW STRUCTURES

by

William K. Hudson

A thesis

submitted in partial fulfillment

of the requirements for the degree of

Master of Science in Geophysics

Boise State University

December 1997

REPORT DOCUMENTATION PAGE

Form Approved
OMB No. 0704-0188

1. AGENCY USE ONLY *(Leave blank)*	2. REPORT DATE	3. REPORT TYPE AND DATES COVERED
	~~4/27/98~~	Final

4. TITLE AND SUBTITLE
Geophysical Measurements of Basalt Intraflow Structures

5. FUNDING NUMBERS
N00014-92-J-1143

6. AUTHOR(S)
William K. Hudson

7. PERFORMING ORGANIZATION NAMES(S) AND ADDRESS(ES)
Center for Geophysical Investigation of the Shallow Subsurface
Boise State University
1910 University Drive
Boise, Idaho 83725

8. PERFORMING ORGANIZATION REPORT NUMBER

9. SPONSORING / MONITORING AGENCY NAMES(S) AND ADDRESS(ES)
Office of Naval Research
800 N Quincy Street
Arlington, VA 22217-5000

10. SPONSORING / MONITORING AGENCY REPORT NUMBER

11. SUPPLEMENTARY NOTES

a. DISTRIBUTION / AVAILABILITY STATEMENT
Approved for public release; distribution unlimited

12. DISTRIBUTION CODE

13. ABSTRACT ***(Maximum 200 words)***

14. SUBJECT TERMS
geophysical properties of basalt

15. NUMBER OF PAGES
96

16. PRICE CODE

17. SECURITY CLASSIFICATION OF REPORT	18. SECURITY CLASSIFICATION OF THIS PAGE	19. SECURITY CLASSIFICATION OF ABSTRACT	20. LIMITATION OF ABSTRACT
UNCLASSIFIED	UNCLASSIFIED	UNCLASSIFIED	

GEOPHYSICAL MEASUREMENTS OF BASALT INTRAFLOW STRUCTURES

by

William K. Hudson

A thesis

submitted in partial fulfillment

of the requirements for the degree of

Master of Science in Geophysics

Boise State University

December 1997

This thesis presented by William K. Hudson

entitled Geophysical Measurements of Basalt Intraflow Structures

is hereby approved:

Paul Michaud 11/26/97

Advisor Date

John R. Pelton 12-2-97

Committee Member Date

Craig Smith 12-2-97

Committee Member Date

K M Hollenbaugh 12-5-97

Graduate Dean Date

ABSTRACT

Basalt is a common constituent in the subsurface throughout much of the Pacific Northwest. As such, the physical properties of basalt are relevant to engineering and hydrogeology in the region. The physical properties of basalt can change dramatically within a single flow and may be associated with changes in intraflow structure. The purpose of this thesis was to make geophysical measurements of a basalt flow and interpret them in terms of available geologic information. It is hoped that these results will be of value in future research to characterize basalt intraflow structures, such as efforts to remotely determine fracture densities and infilling materials.

The basalt of Lucky Peak is a thick flow that exhibits common intraflow structures in outcrop. Geophysical data were collected near the outcrop, and the results of data analysis were compared to the outcrop. The primary geophysical methods used were vertical seismic profiling and cross-borehole ground penetrating radar. Secondary geophysical methods used were transient electromagnetism (TDEM), Schlumberger resistivity, and the measurement of hand sample dielectric permittivity. In addition, petrographic descriptions and measurement of fracture characteristics were performed on core samples, and a magnetic field experiment was conducted to confirm the extent of basalt beneath the study site.

The basalt of Lucky Peak, which originated along the south fork of the Boise River near Smith Prairie, filled the then active river channel and buried an adjacent terrace 20

meters above the active flood plain. Magnetic field strength data show the basalt extends more than 200 meters back from the cliff face just downstream from the Lucky Peak Dam. Visible in outcrop at this location are well developed intraflow structures common to basalt flows throughout the region. Relative elevations of these intraflow structures (flow top, upper colonnade, entablature, and lower colonnade) were measured using a total station survey instrument and converted to absolute elevation above sea level. Elevations of intraflow structures in the subsurface near the outcrop were assumed equal to the elevations in outcrop. Electrical resistivity profiles made using TDEM and Schlumberger methods clearly show the contact between the overlying sediments and the basalt, but they do not show contrasts in resistivity within the basalt flow.

Core was taken from the basalt of Lucky Peak approximately 35 meters back from the cliff face. Three additional boreholes were also drilled at this location. Fracture characteristics determined from core do not show strong correlation with fractures seen in outcrop. Overall fracture density measured on core is greatest in the upper colonnade and lowest in the lower colonnade. Thin sections made from core show increased glass content in the entablature compared to the upper and lower colonnade. Dielectric permittivity measurements on hand samples from core do not show strong correlations with intraflow structure.

Cross-borehole ground penetrating radar data show that the entablature of the basalt of Lucky Peak has lower velocity than does the upper or lower colonnade, although the difference cannot be called statistically significant. Attenuation analysis of the radar data yields contradictory information. Data records reveal lower signal to noise ratios in the

entablature compared to the upper and lower colonnade. Amplitude spectra from the records show a nearly complete loss of signal above ~50 MHz in the entablature which is not seen in the other intraflow structures. However, the spectral ratio method used for calculating radar attenuation yields results indicating less attenuation in the entablature compared to the upper and lower colonnade. This apparently contradictory result is attributed to the loss of coherent signal within the entablature. The resulting ratio of noise amplitudes is misleading, and the validity of the spectral ratio results is discounted. Based on visual inspection of data records and amplitude spectra, radar wave attenuation is highest in the entablature.

Vertical seismic profile data show that the entablature and lower colonnade have higher seismic velocity (both P- and S-wave) and lower P-wave attenuation than the upper colonnade and flow top (S-wave attenuation calculations were not done). These results correlate with a general decrease in fracture density measured in core from the upper colonnade through the entablature to the lower colonnade. Although the results were not what was expected based on fracture characteristics observed in outcrop, they are consistent in showing high velocity in zones of low attenuation, and low velocity in zones of high attenuation.

ACKNOWLEDGMENTS

During the summer of 1988, I decided to attain a graduate degree and a career in the field of environmental sciences. Nine and a half years later, after many starts and mis-starts, I have finally reached my goal. The premier product of this quest, namely this thesis, is the culmination of five years of education at Boise State University. I acknowledge two persons in particular for allowing my start at BSU. First, I thank my very good friend Terri Nelson, whose timely faith in me put me in a position to accept the opportunity offered here. Second, I thank Dr. Jack Pelton for offering me a graduate assistantship with the Center for Geophysical Investigation of the Shallow Subsurface at a time when I wasn't even sure what geophysics was.

Along the way, many individuals aided my education at BSU, either by offering pertinent information or by listening to the rants of a frustrated graduate student. In the former category I acknowledge Dr. Paul Donaldson and Dr. Craig White for giving me "short courses" on their respective subjects for inclusion in this thesis, and Lee Liberty for providing insights into the workings of UNIX (without resorting to "RTFM"). In the latter category I give special acknowledgment and thanks to R. D. Bolger and Susan Kay-Dittus who were with me the whole way. And, I would be remiss if I did not acknowledge in both categories Dr. Martin Dougherty, whose grant funded the majority of my research.

Several persons outside the university were instrumental in my thesis work. I acknowledge the Steele family of Boise, Idaho, who gave permission for the project to proceed on their land. I thank Dennis Barker, Project Manager, Bechtel Nevada Corporation, and Steve Molnar, Geophysical Engineer, Powder River Geophysical, for the long hours they spent at my site collecting the borehole radar data that is a major part of this thesis. I also acknowledge the invaluable help of Dr. Indira Chatterjee and Dana McPherson, Department of Electrical Engineering, University of Nevada, Reno, for the measurements of dielectric permittivity on the basalt hand samples.

Finally, I acknowledge and thank Dr. Paul Michaels, who, besides helping collect and process the seismic data included herein, took control of my thesis committee in mid-stream and provided the direction and mathematical rigor necessary to bring it to completion. To all these persons, and to the many others who helped and are not listed, I express my sincere gratitude.

ABSTRACT

Basalt is a common constituent in the subsurface throughout much of the Pacific Northwest. As such, the physical properties of basalt are relevant to engineering and hydrogeology in the region. The physical properties of basalt can change dramatically within a single flow and may be associated with changes in intraflow structure. The purpose of this thesis was to make geophysical measurements of a basalt flow and interpret them in terms of available geologic information. It is hoped that these results will be of value in future research to characterize basalt intraflow structures, such as efforts to remotely determine fracture densities and infilling materials.

The basalt of Lucky Peak is a thick flow that exhibits common intraflow structures in outcrop. Geophysical data were collected near the outcrop, and the results of data analysis were compared to the outcrop. The primary geophysical methods used were vertical seismic profiling and cross-borehole ground penetrating radar. Secondary geophysical methods used were transient electromagnetism (TDEM), Schlumberger resistivity, and the measurement of hand sample dielectric permittivity. In addition, petrographic descriptions and measurement of fracture characteristics were performed on core samples, and a magnetic field experiment was conducted to confirm the extent of basalt beneath the study site.

The basalt of Lucky Peak, which originated along the south fork of the Boise River near Smith Prairie, filled the then active river channel and buried an adjacent terrace 20

meters above the active flood plain. Magnetic field strength data show the basalt extends more than 200 meters back from the cliff face just downstream from the Lucky Peak Dam. Visible in outcrop at this location are well developed intraflow structures common to basalt flows throughout the region. Relative elevations of these intraflow structures (flow top, upper colonnade, entablature, and lower colonnade) were measured using a total station survey instrument and converted to absolute elevation above sea level. Elevations of intraflow structures in the subsurface near the outcrop were assumed equal to the elevations in outcrop. Electrical resistivity profiles made using TDEM and Schlumberger methods clearly show the contact between the overlying sediments and the basalt, but they do not show contrasts in resistivity within the basalt flow.

Core was taken from the basalt of Lucky Peak approximately 35 meters back from the cliff face. Three additional boreholes were also drilled at this location. Fracture characteristics determined from core do not show strong correlation with fractures seen in outcrop. Overall fracture density measured on core is greatest in the upper colonnade and lowest in the lower colonnade. Thin sections made from core show increased glass content in the entablature compared to the upper and lower colonnade. Dielectric permittivity measurements on hand samples from core do not show strong correlations with intraflow structure.

Cross-borehole ground penetrating radar data show that the entablature of the basalt of Lucky Peak has lower velocity than does the upper or lower colonnade, although the difference cannot be called statistically significant. Attenuation analysis of the radar data yields contradictory information. Data records reveal lower signal to noise ratios in the

entablature compared to the upper and lower colonnade. Amplitude spectra from the records show a nearly complete loss of signal above ~50 MHz in the entablature which is not seen in the other intraflow structures. However, the spectral ratio method used for calculating radar attenuation yields results indicating less attenuation in the entablature compared to the upper and lower colonnade. This apparently contradictory result is attributed to the loss of coherent signal within the entablature. The resulting ratio of noise amplitudes is misleading, and the validity of the spectral ratio results is discounted. Based on visual inspection of data records and amplitude spectra, radar wave attenuation is highest in the entablature.

Vertical seismic profile data show that the entablature and lower colonnade have higher seismic velocity (both P- and S-wave) and lower P-wave attenuation than the upper colonnade and flow top (S-wave attenuation calculations were not done). These results correlate with a general decrease in fracture density measured in core from the upper colonnade through the entablature to the lower colonnade. Although the results were not what was expected based on fracture characteristics observed in outcrop, they are consistent in showing high velocity in zones of low attenuation, and low velocity in zones of high attenuation.

TABLE OF CONTENTS

LIST OF FIGURES

1. INTRODUCTION

1.1 Basalts and Human Activity

1.1.1 Basalts of the Pacific Northwest

Basalt is a major geological constituent of the Columbia River Plateau and Snake River Plain. Lavas of the Miocene Columbia River Basalt Group cover an area of approximately 200,000 km^2 in eastern Washington, eastern Oregon, and west-central Idaho. Miocene-Recent Snake River basalts cover an area greater than 20,000 km^2 from south-central to south-eastern Idaho (Mabey, 1982). Young basalt flows less than a million years old occur on the surface over much of the Snake River Plain, and older flows are exposed throughout the region in road cuts and river canyons. Although loess and other sediments cover lavas in parts of the Columbia Plateau and Snake River Plain, basalt is still the major rock type in the shallow subsurface in these areas. In the eastern Snake River Plain, the total thickness of basalt may be as much as 1 kilometer (Whitehead, 1992); in the Columbia Plateau, the average thickness of the basalt is greater than 1 kilometer (Myers and Price, 1979).

1.1.2 Motivation for Geophysical Characterization of Basalt

Because basalt flows are so prevalent in the region, they often have direct influence on the activities of humans. The regional aquifer systems that supply water for irrigation in the Columbia River Plateau and eastern Snake River Plain are primarily in basalt (Whitehead, 1992, Whiteman et al., 1994). Engineering projects, such as road, tunnel and

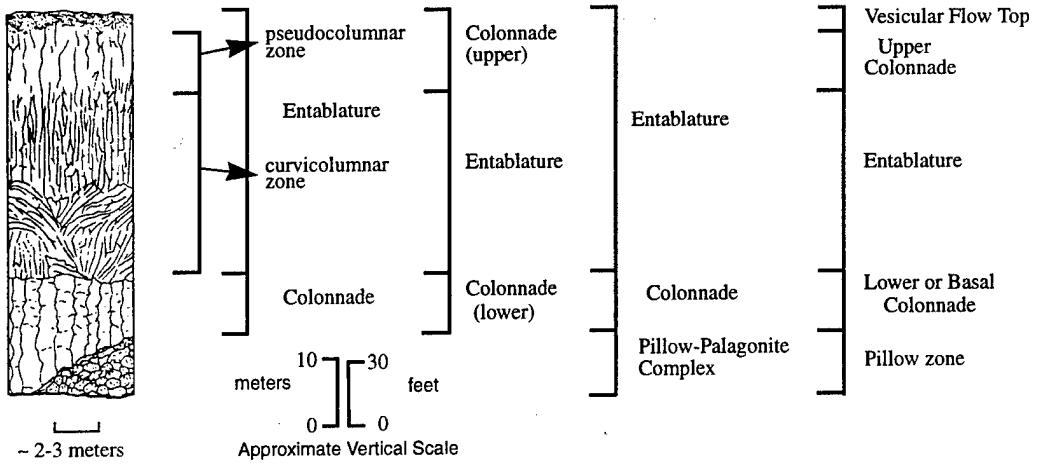

Figure 1.1 Typical intraflow structures of thick basalt flows, and the nomenclature used in previous studies (from Long and Wood, 1986). Fractures are represented in stylized manner; fracture widths are not to scale. Nomenclature in this thesis will follow the usage of Long and Davidson (1981).

building construction, must be planned to account for basalt throughout most of the region. At the Hanford Nuclear Reservation in eastern Washington, and the Idaho Nuclear Engineering Laboratory in eastern Idaho, the storage and disposal of radioactive wastes is done directly on and in basalt flows. Understanding the characteristics of basalt flows will help in designing future projects, as well as mitigating the damage done by past activities.

1.2 Intraflow Structure

1.2.1 Cooling Joints

Intraflow structure is defined as the differentiation of physical features that develops within a *single* flow of basalt as the molten lava cools. Figure 1.1 shows examples of

intraflow structures common to thick flows of the Columbia River and Snake River basalt groups. Long and Wood (1986) write:

> Colonnade typically occurs in the lower third of a flow and consists of relatively well-formed basalt columns. These columns are commonly perpendicular to the base of the flow and range in width from ~0.3-2 meters. The entablature overlies the lower, or basal, colonnade and typically occupies the interior one-third to upper one-half of the flow. Entablature has small (0.2 to 0.5 meter diameter), irregular to hackly columns, which may form radiating patterns or otherwise deviate from an orientation perpendicular to the base of the flow. Entablature commonly gives way upward to upper colonnade, which in turn grades to a vesicular flow top.

Long and Wood (1986) describe how intraflow structures can be explained in terms of differences in the methods and rates of cooling. Slow cooling resulted in the well developed columns at the bottom of a flow. The upper colonnade, below the rubbly flow top, also underwent gradual cooling, though it typically formed less well defined columns than the lower colonnade. Long and Wood (1986) theorize that the smaller, more randomly oriented columns of the entablature were created when the lava was quenched by surface water. Long (personal communication, 1995) theorizes that streams dammed by lava flows re-emplaced themselves over the top of the flows, providing the water for quenching. This water infiltrated through fractures in the upper colonnade and significantly increased the rate of cooling in the flow interior, resulting in smaller columns. Long and Wood (1986) describe how these differential cooling rates also resulted in petrographic texture differences between the intraflow structures.

1.2.2 Bulk Properties of Basalts

Basalt flows in the Columbia River Plateau and Snake River Plain differ in age and composition, but they share many characteristics. On local and regional scales, the intraflow structure in basalt controls bulk properties. These properties include hydraulic conductivity and rock strength in tunnels (Whitehead, 1992; Lindberg, 1989). For example, in the eastern Snake River Plain, flows consist of intertwining "fingers" of basalt. Each finger is a small stream of lava which may be tens of meters wide and deep, and hundreds of meters long. These fingers have highly vesicular, rubbly flow tops, which were buried by successive fingers of the same, or later, flows. Water movement in these rubble zones is several orders of magnitude greater than in the massive, central zones of each finger (Whitehead, 1992). Similar contrasts in bulk properties are also found between other intraflow structures.

1.3 Geophysical Characterization of Basalt

1.3.1 Previous Research

Only limited research has been done in the past to use geophysics to characterize basalt intraflow structure. Miller and Steeples (1990) conducted a shallow seismic reflection experiment in the basaltic terrain of the eastern Snake River Plain. They report the successful imaging of a sedimentary layer at approximately 30 meters depth, although considerable processing of the data was required to compensate for extreme variations in overburden composition and thickness (Miller and Steeples, 1990). Dougherty et al. (1995) conducted surface and borehole ground penetrating radar (GPR) experiments in the basalt of the eastern Snake River Plain. A vesicular layer in the flow was successfully

mapped in the subsurface away from a cliff face by surface GPR. Borehole GPR showed less conclusive results, although zones of velocity and attenuation contrasts were visible in the data (Dougherty et al., 1995).

1.3.2 Research Goals

The chief goal of this thesis was to compare the measured geophysical properties of a basalt flow with intraflow structures observed in outcrop. Primary emphasis was given to interpreting results from cross-borehole ground penetrating radar and vertical seismic profile experiments. Data collected with these methods near the outcrop were analyzed to show changes in the velocity and attenuation of the respective energy forms as a function of elevation in the subsurface. Elevations of the intraflow structural contacts in the outcrop were determined, allowing for comparison of geophysical properties and intraflow structures based on elevation.

For further comparison, additional geologic and geophysical data were collected as a function of elevation. Geologic stratigraphy was determined from driller's logs. Fracture characteristics in the subsurface were determined from core taken near the outcrop, and petrograhic descriptions were compiled of thin sections made from core. Dielectric permittivity was measured on core hand samples. Electrical resistivity of the flow was measured using transient electromagnetic field and Schlumberger resistivity methods. The results from each of these methods, along with the radar and seismic interpretations, were then used to show differences in geophysical properties between the intraflow structures.

2. GEOLOGY AND CORE DATA

2.1 Geology of the Study Site

2.1.1 The Basalt of Lucky Peak

The basalt of Lucky Peak (BLP) was selected for this thesis. Aside from its close proximity to Boise, it has several features that make it ideal for the current investigation. BLP has considerable exposure in outcrop and does not contact other basalt flows. There is very little development in the vicinity, so cultural noise is minimal. The relative thickness of the flow is analogous to the thick flows common in the Columbia River Plateau. In addition, the relatively young age of the flow minimizes complications from secondary structure in the formation.

Howard et al. (1982) named the basalt of Lucky Peak for the thick (~40 meter) canyon-filling basalt flow that forms the north canyon wall of the Boise River just downstream from the Lucky Peak Dam. At this location, the BLP is continuously exposed in four kilometers (km) of the cliff face (Figure 2.1). Howard et al. (1982) give the source of this flow as being along the South Fork of the Boise River, in the vicinity of Smith Prairie, Idaho. BLP filled the channel of the ancestral Boise River, burying the active flood plain and an adjacent terrace approximately 20 meters above the active flood plain (Othberg and Burnham, 1990, and Othberg, 1994) (Figure 2.2).

In places at the base of the cliff, the bottom of the basalt flow is exposed. At these locations, the gravel sediments on which the basalt was emplaced are clearly visible. At

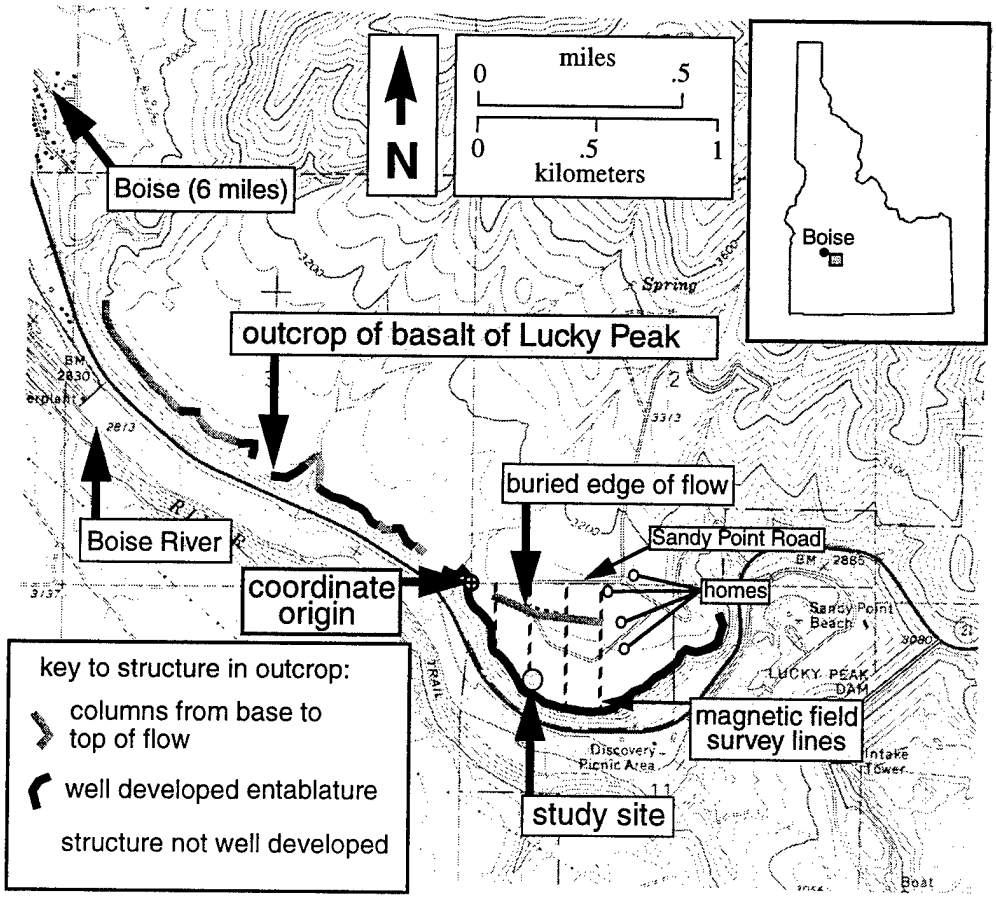

Figure 2.1 Location map of study site and surrounding area. The basalt of Lucky Peak is exposed in the north canyon wall of the Boise River just downstream from the Lucky Peak Dam, approximately 6 miles from downtown Boise, Idaho. Well developed intraflow structure is visible in outcrop, the locations of the various structures are shown in the figure. The study area is located on the terrace formed by the basalt of Lucky Peak (T2N, R3E, sec. 11), approximately 1 km from the dam. Inset shows location of figure relative to Boise and the state of Idaho. The "coordinate origin" is the brass monumnet marking the northwest corner of section 11 and is the origin of the coordinate axis used in this study . The line depicting the buried edge of the basalt in interpreted from magnetic field data which were collected along the lines shown (see text, 2.1.4). (Base map from Lucky Peak Quadrangle, USGS, 1972).

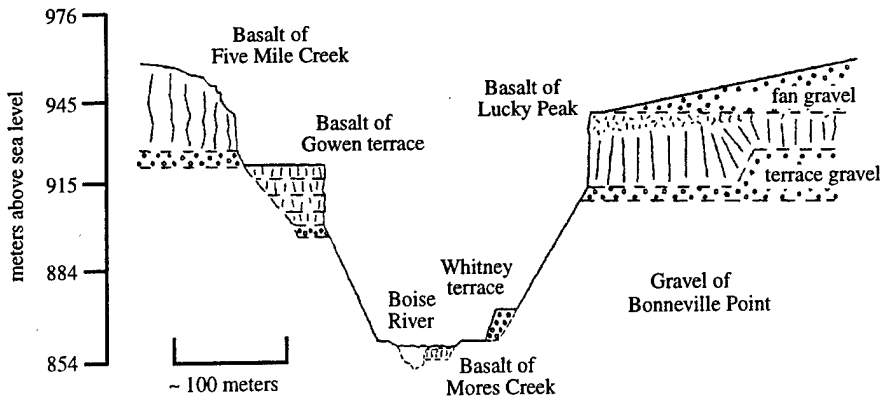

Figure 2.2 Profile and cross section of the Boise River canyon near Lucky Peak Dam (from Othberg, 1994). Diagramed is a simplified cross section along an approximate north-south line. The basalt of Lucky Peak is located in the north canyon wall, isolated from other basalt flows. The step in the base of the basalt of Lucky Peak represents where the flow buried the active flood plain as well as an adjacent terrace at the time of emplacement.

some locations, it is possible to find cobbles which were embedded in the flow itself while the magma was fluid. At the eastern most extent of the flow, across from the Lucky Peak Dam, evidence can be seen of the basalt burying the active river channel and adjacent terrace, as described by Othberg (1994). Here, the base of the flow can be followed from a higher gravel terrace down a slope to a lower gravel terrace. Columns in the basalt are perpendicular to this slope, indicating the cooling front was parallel to it.

Potassium-argon (K/Ar) dating techniques, magnetic polarity data, and stratigraphic information yield conflicting results for the age of BLP. Howard et al. (1982) obtained a K/Ar age for BLP of 2.1 ± 0.5 million years (Ma). This places the eruption during the Matuyama reverse polarity chron. However, BLP has normal remanent polarity (Howard

et al., 1982) which is thus anomalous with this age (Othberg and Burnham, 1990). Othberg and Burnham (1990) summarized the results of other K/Ar dates that place the age at 1.364 ± 0.21 Ma; however, they considered this to be too old based on their interpretation of stratigraphy. Using stratigraphy and K/Ar dating of other basalt flows in the area, Othberg and Burnham (1990) and Othberg (1994) placed the minimum age of BLP at 0.572 Ma. The normal polarity of the flow suggest a maximum age of 0.730 Ma, the boundary between the Brunhes normal and Matuyama reverse polarity chrons (Othberg and Burnham, 1990).

2.1.2 Study Site Description

The study site is located approximately 1 km west of the Lucky Peak dam, on the relatively flat terrace formed by BLP (Figure 2.1 and Figure 2.2). Ground cover at this site is primarily wild grasses and sage brush. Overburden above the basalt flow consists of reworked gravels from the surrounding highlands and loess, in which primitive soils have developed (Othberg and Burnham, 1990). A calcic B horizon was noted by Othberg and Burnham (1990). The Corps of Engineers (1948) also described a calcic layer on this terrace:

> A caliche layer of 3 feet average thickness was encountered at a depth of three to four feet below the ground surface, generally at the boundary of the silt and gravel zones. In some cases this stratum is soft, but more generally it is hard to very hard. This material is so hard that a hand pick does not remove it readily (U.S. Army Corps of Engineers, 1948).

Evidence of this caliche layer was seen in drill cuttings and core. It's presence may account for results in electrical resistivity profiles as well as the lack of radar signal seen in the first few meters of depth in the subsurface.

Four homes are located on the terrace at a distance of 400-600 meters from the study area (Figure 2.1). Electrical power and phone lines servicing these homes run along Sandy Point Road, and are more than 400 m from the study site. Other electrical power and phone lines run along the highway, next to the river (Figure 2.1). These utilities are at a distance greater than 100 meters laterally, and 70 meters below the study site on the terrace.

2.1.3 Well Driller's Reports and Borehole Logs

Driller's notes were obtained for the water wells servicing the houses labeled a, b, and d in Figure 2.1. Elevations for the wells were estimated from Figure 2.1. "Well d" in Figure 2.1 penetrates ~27 m of basalt between 940 and 914 meters elevation, this is assumed to be BLP. Below this is 7 m of sand and gravel before encountering another basalt at 907 m elevation, assumed to be Tertiary basalt volcanic assemblage (Tbv) (Othberg, 1994). "Well b" does not encounter BLP, it passes through alternating layers of sands and gravels before hitting basalt at ~920 m elevation. The water table in both wells was approximately 97 m below land surface, the approximate level of the Boise River. "Well a" encounters basalt at 943 m elevation, which is near the elevation of BLP. However, the driller's report describes this elevation as the start of alternating layers of red, black, and red & black basalts, which is consistent with interpretations of Tbv in the reports of the other wells. The marked change in elevation of the top of Tbv between

wells a and b is attributed to a fault passing east-west between these wells (Othberg, 1994).

At the study site, three air rotary and one cored boreholes were drilled. Figure 2.3 shows the location of these boreholes relative to the cliff. The coordinates in the figure are relative to the north-west corner of section 11 (Figure 2.1), which was assigned the arbitrary x-y position, in meters, of [10,000 10,000]. Distances were then measured positive north and positive east. The well field is approximately 300 meters east, and 400 meters south of the section corner. Borehole number 1 (BH1) is the cored hole, the others are air rotary holes. Drilling of each borehole was stopped when the bit broke through the base of the basalt and into sands and cobble gravels, approximately 32 meters below land surface.

The driller's reports confirm BLP overlies and is emplaced against terrace gravels as described by Othberg (1994) (Figure 2.2), and that the buried edge of BLP must be between wells b and d (Figure 2.1). The driller's reports also indicate that the water table is well below the base of BLP. Borehole drilling also confirmed the presence of gravels beneath BLP. Notes from the borehole drilling show the overburden thickness at the study site to be ~2 meters, and the bottom of the flow to be ~32 meters below land surface. Overburden consists of soil overlying a caliche layer. Inspection of BH1 core indicates the caliche has infiltrated the rubble layer of the BLP to a depth of ~7 meters below land surface (935 meters elevation).

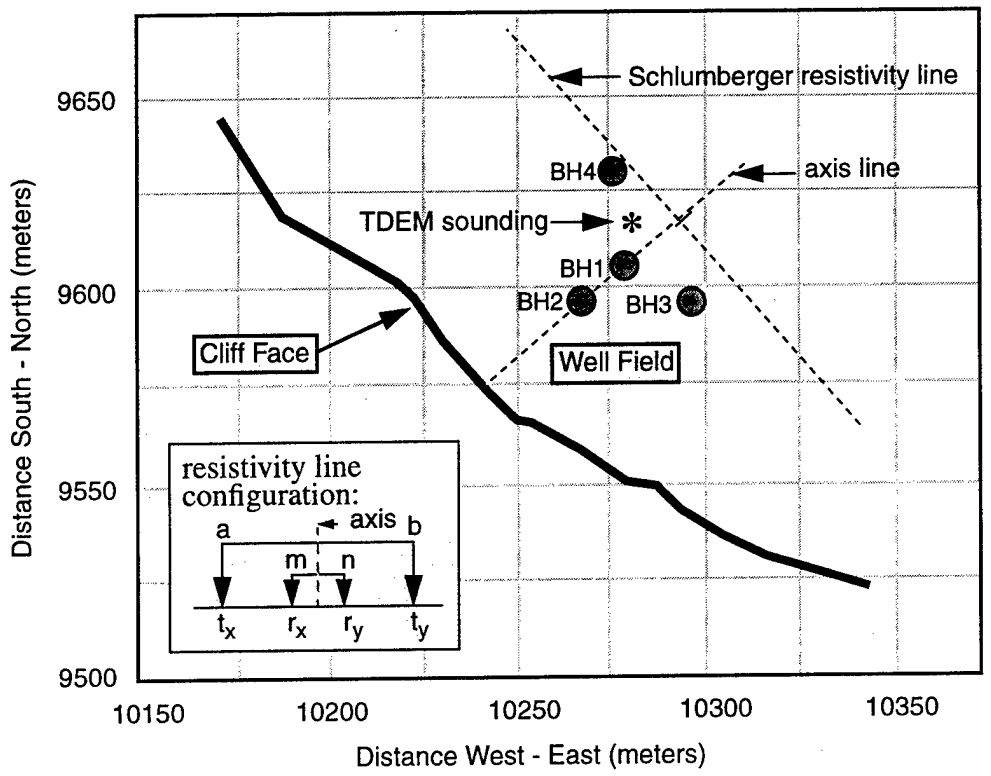

Figure 2.3 Well field map. Shown are the locations of the boreholes and the electromagnetic experiments relative to the cliff face. The origin of the coordinate axes is the north-west corner of section 11 (Figure 2.1). BH1 was cored; BH2, BH3, and BH4 were air rotary drilled (note: borehole diameters not to scale). The "axis line" of the well field is defined as passing through BH1 and BH2. A Schlumberger resistivity experiment was conducted perpendicular to, and centered on, this axis line. Transmitter antenna were placed at t_x and t_y, receivers were placed at r_x and r_y. The distance ab/2 is used to plot the resistivity data in Figure 2.10. A time domain electromagnetic sounding was conducted at the point indicated.

2.1.4 Magnetic Field Data

Anomalies in magnetic field strength data were analyzed in an effort to locate the buried edge of the basalt flow and confirm that it is well away from the study area. Basalt has a relatively higher iron content compared to the surrounding gravels, and has a correspondingly higher remanent magnetization. In a line running across the terrace, away from the cliff face, a higher magnetic field strength at the surface is expected when the line is over the basalt flow, lower magnetic field strength is expected after the line crosses over onto the surrounding gravels.

Magnetic field strength data were collected using a Geometrics G 816 magnetometer. Four lines, 100 meters apart, were staked out, beginning at the cliff near the study site, and running north approximately to Sandy Point Road (Figure 2.1). Data were collected along these lines at stations spaced 10 meters apart. Data collection took less than four hours; background readings were taken approximately every 45 minutes at a base station.

Figure 2.4 is a plot of the magnetic field strength, in gammas, of the four data collection lines. Background drift was 25 gammas over the course of the experiment, Background drift corrections were not made on the data. In addition, because only an approximate boundary of the basalt was needed, data were not corrected for field inclination. Magnetic field strength values are plotted in Figure 2.4 as a function of position relative to the coordinate system described above. Each line begins, on the left side of the plot, at the cliff edge, and ends on the right side approximately at Sandy Point Road (Figure 2.1).

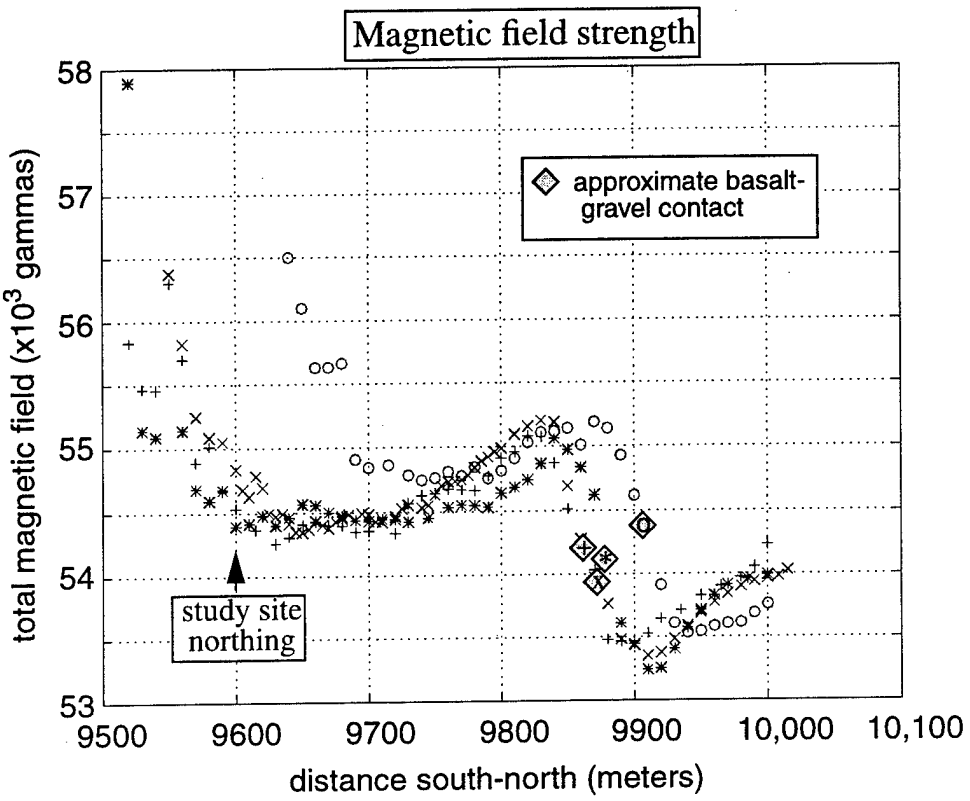

Figure 2.4 Magnetic field strength along four lines near the study area. Positions of the data collection lines are shown in Figure 2.1. Data were collected at stations spaced 10 meters apart along four north-south lines which were 100 meters apart. Distance is relative to the coordinate origin (Figure 2.1). Each line begins at the cliff edge, which is at the extreme left of each line of data in the plot. Between ~9800 and 9950 meters each line shows a rise in field strength, followed by a fall and subsequent rise. This is interpreted as an edge effect caused by the contact of the basalt of Lucky Peak with the gravel formations of the adjacent highlands (Figure 2.2). The center of the fall in field strength is interpreted as the approximate contact between basalt and gravels.

The data in Figure 2.4 show high magnetic field strength close to the cliff face, where basalt is exposed on the surface. Away from the cliff, overburden increases and field strength decreases. A characteristic edge effect in the magnetic field strength is evident in all four lines between approximately 9800 and 9950 meters. This effect is seen, from left to right, as a rise in field strength, then a sharp drop, followed by a rebound to a lower value than before the first rise. The effect is characteristic of a sharp change in magnetic susceptibility of underlying beds (Telford et al., 1990), in this case a basalt flow to a gravel formation. The buried edge of the basalt is interpreted as being near the midpoint of the fall in magnetic field strength along each line.

The purpose of these magnetic field measurements was to confirm that the basalt was continuous under the study site. For the purposes of this study, the location of the basalt-gravel contact is approximately at the mid-point of the fall in field strength, and these positions are marked with diamonds in Figure 2.4. These mid-points were interpolated into the line shown in Figure 2.1 for the buried edge of basalt. This line shows the basalt-gravel contact striking approximately east-west near the study site. Determining the precise location of the basalt-gravel contact relative to the fall in field strength would require correcting for field inclination and modeling of the cross sectional shape of the contact, which was not done on the data in Figure 2.4.

2.2 Outcrop Data

2.2.1 Occurrence of Intraflow Structure

The outcrop of the basalt of Lucky Peak is approximately 4 km in length (Figure 2.1). Well developed intraflow structures are seen throughout most of this distance. In

approximately one third of the outcrop, well developed columns (~1-2 m diameter) extend from the base to the top of the flow. Well developed entablature is seen in nearly half the length of the outcrop, the most extensive occurrence is at the eastern end. At each end of this occurrence, entablature thins to less than 1/3 of flow thickness; near the center of this occurrence, approximately adjacent to Discovery Park (Figure 2.1), the flow is at its maximum thickness (~40 m) and the entablature comprises approximately 2/3 of flow thickness.

2.2.2 Elevations of Intraflow Structures

Figure 2.5 shows a photograph of the outcrop at the study area. Labeled in the photograph are the lower colonnade, entablature, upper colonnade, and flow top/rubble zone. Elevations of these structures were measured using a Topcon total station survey instrument. In order to get the position of the structural contacts, the target prism of the survey system was lowered over the side of the cliff attached to a flat board with a rope. At the appropriate elevation the target was held stationary, and a measurement taken. The relative elevations from this survey were converted to absolute elevations above sea level using the elevation given for the intersection at the west end of Sandy Point Road on the Lucky Peak quadrangle map (USGS, 1972). The elevation of the land surface in the center of the study site, near the truck in the Figure 2.5, is 941 meters above sea level.

BLP is approximately 29 meters thick in outcrop at the study site. The lower colonnade and entablature are approximately 8 and 9 m thick, respectively; the upper colonnade and flow top/rubble are approximately 8 and 4 m thick, respectively. The flow top/rubble layer varies in thickness up to +/- 1 m over the distance of a few meters along

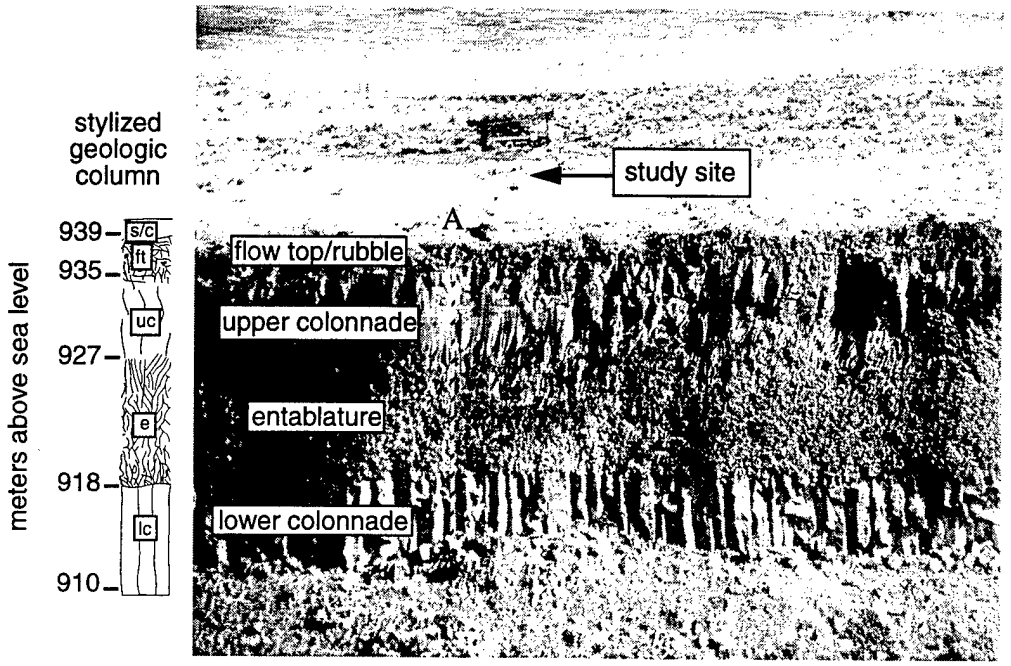

Figure 2.5 Photograph of basalt of Lucky Peak at the study site. The study site is located approximately 35 meters from the cliff face. Well developed intraflow structures is visible in the outcrop. Elevations of intraflow structures were measured approximately along A-A'. A stylized geologic column was drawn from the photograph. The elevations and stylized geologic column are used throughout this thesis for reference and comparison to the data presented. In the geologic column the following abbreviations are used: s/c = soil caliche, ft = flow top, uc = upper colonnade, e = entablature, lc = lower colonnade.

the cliff edge, the thickness of 4 meters is close to the maximum observed. Using the elevation of the flow top at the cliff face, the thickness of the overburden in the well field is estimated to be two meters, which is consistent with driller's notes (section 2.1.3).

2.3 Core Data

2.3.1 Reconstruction of BH1 Core

A core was taken from the basalt of Lucky Peak at the location of BH1 in Figure 2.3. A six inch hole was rotary drilled through the overburden until hard basalt was encountered at ~2 m below land surface (7 ft. below land surface). Steel casing was installed to this depth. Core was then taken from ~2 m below land surface to a total depth of 32 m below land surface (~30.5 meters of core total). The core tube was ~1.5 m (5 ft) in length, this was the maximum length of a drill run. At the end of each drill run, the driller measured the distance from land surface to the bottom of the run. This was marked on wooden blocks and placed at the end of the core segment after it was placed in the core box. Nine core boxes were used to hold the core.

The core was reconstructed in three meter long lengths of angle iron. In general, because there was considerably more rubble in the top few meters, the bottom of the core was more easily reconstructed than the top. Therefore, reconstruction was done from the bottom up. Relative orientation of the core pieces was reliably maintained through the lower two thirds of the flow (0 - ~21 meters above base of core). Above this depth, short segments of core (up to 1 m in length) were reliably pieced together, but the relative orientations of these segments to the whole core could not be determined. When reconstruction was complete, a chalk line was snapped along the top of the core as it lay in

the angle iron troughs. This axis line was then remarked with indelible ink. Approximately 0.5 cm from bottom of the core, a cross-line was drawn and labeled zero. Positions on the core were then measured positively upward along the axis line from this zero line.

At the top of the core, where rubble prevented reliable reconstruction, distances measured along the core did not agree with distances calculated from the driller's notes on the wooden blocks stored with the core. Where this occurred, the position scale on the core was adjusted to reflect the position inferred from the driller's notes. This results in the relative positions of features in these segments being accurate, but it does not account for the discrepancies in distance between segments.

2.3.2 BH1 Core Fracture Observations

Fracture density and orientation data were recorded from BH1 core in an attempt to find patterns corresponding to intraflow structure seen in outcrop. Previous researchers did comparisons of fracture characteristics in outcrop and core in Columbia River Basalt and generally failed to find a relationship between fractures seen in outcrop and those seen in core taken nearby (cf. Long, 1978; Long et al., 1980; Long and Davidson, 1981; Meints, 1986). One notable exception is in Type III flows, which are defined as thick flows with well developed lower colonnade and entablature meeting at a single, sharply defined contact (Long, 1978). In outcrop, Type III flows show a sharp decrease in the average fracture density (number of fractures per meter) below the entablature-colonnade contact. In core, a corresponding decrease in the average fracture density is also seen, though the change is less pronounced (Long and Davidson, 1981). Since the basalt of

Lucky Peak is a Type III flow; it was expected that a change in fracture density would be seen at positions in the core that correspond to intraflow structure seen in outcrop.

The stratigraphic height of every fracture that crosses the reference line on the core was measured to the nearest 0.001 m. The measurements were then written in indelible ink on the core next to the fracture. The fine scale of measurement was necessary to distinguish closely spaced fractures, however, due to gaps in the reconstruction of core, the absolute position of any one fracture is not this precise. Near the bottom of the core, the error in height above the base is estimated to be less than 0.020 m (2 cm); near the top the error is estimated to as much as 0.250 m (25 cm). Estimates of the percentage of infilling by secondary minerals in each fracture were also recorded (from zero, for no infilling to 100% for fracture faces completely covered with infilling material). Some of the fractures showed freshly broken faces that were obviously caused by drilling. These were recorded as driller's breaks and were excluded from the fracture counts.

Measurements were made of the angle of each fracture relative to the core axis and the strike of the fracture relative to the reference line. A measurement was made either of the greatest distance across the fracture face, or of the length of the fracture along the axis of the core. These measurements were made to the nearest 0.001 m. Using these measurements and the known diameter of the core, the angle from the core axis to the fracture face was calculated. Fracture strike angle was measured relative to the reference line by placing a protractor across the core and measuring the angle to the peak or trough of the fracture from the reference line. This angle was measured to the nearest 10°.

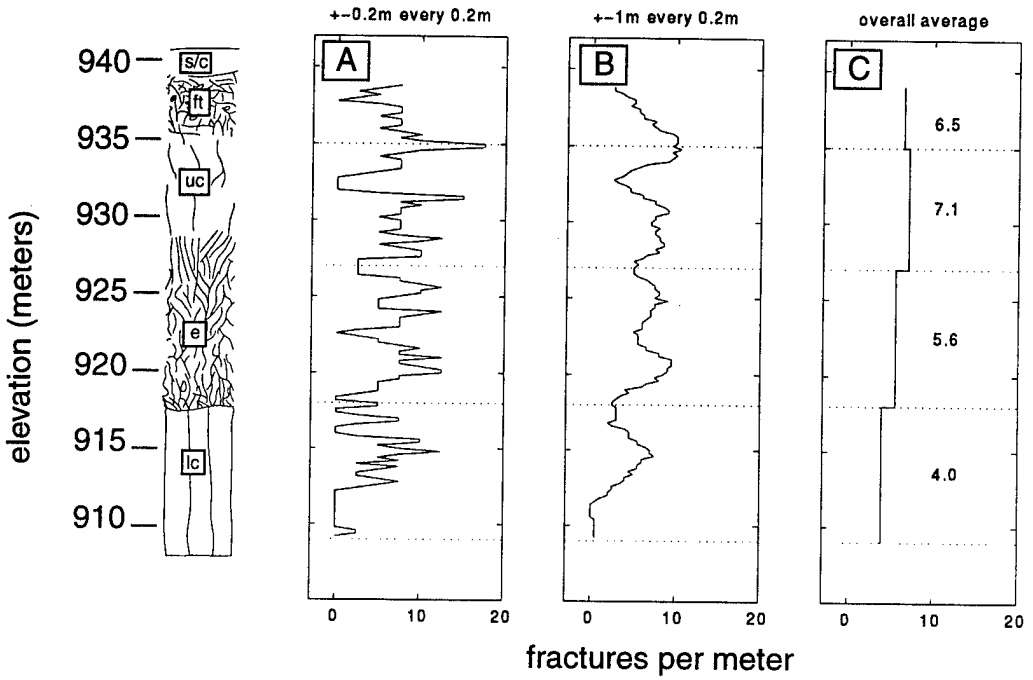

Figure 2.6 Fractures per meter of BH1 core. Plotted are two running averages of the number of fractures per meter of BH1 core, and the overall average fracture density for each intraflow structure. A stylized geologic column is included for reference. All fractures that crossed the reference line, except driller's breaks, are included in the data. (A) shows the fine scale variation in fracture density throughout the flow, (B) shows a smoothed version of fracture density variability, the overall average (C) is a gross estimate for each intraflow structure.

2.3.3 Fracture Characteristics

Figure 2.6 shows two plots of a running average of fractures per meter calculated from the list of fracture positions, and an overall average for each intraflow structure. In A, fractures are counted in a 0.4 meter window (i.e. +/- 0.2 m), every 0.2 meters along the core. This value is normalized to fractures per meter, and plotted at the center of the window. In B, fractures are counted in a 2 meter window every 0.2 meters along the core; this value is also normalized and plotted at the center of the window. Counts were started and stopped with the window completely on the core to avoid edge effects on the running averages. In C, the overall average was calculated by counting the total number of fractures in each intraflow structure and dividing by the thickness of that structure.

Plot A, in Figure 2.6, shows the considerable scatter in the value of fractures per meter along the core. It also shows those sections of core with greater than 0.4 meters of no fractures (such as positions below 918 m, and at ~933 m elevation). Plot B is essentially a low pass filtered representation of the data, that is, extreme variations in fracture densities over short distances are smoothed out. In B, the low fracture density zone at approximately 933 m elevation is evident. A subtle shift to lower fracture densities can also be seen below approximately 920 meters, although scatter in the values is still significant. It is expected that near the bottom of the flow, in the lower colonnade, fractures are predominantly vertical, therefore, fewer fractures will be encountered in a vertical core. The data in Figure 2.6 confirm this expectation, though not strongly. Plot C shows the overall highest fracture density is in the upper colonnade.

Figure 2.7 is a plot of the angle from vertical of each fracture versus elevation in flow. All fractures are plotted, excluding driller's breaks. Fewer fractures are seen at lower dip angles, especially below ~10°, as is expected in a vertical core. Fewer low angle fractures are also seen below a position of ~918 m, which is also expected in the lower colonnade. Some vertical grouping of fracture angles is seen in the plot, this is a result of the precision with which lengths were measured on core. This grouping becomes more pronounced at higher fracture angles (c.f. the near absence of fractures between 80° and 90°). The overall mean fracture angle and its error are plotted with circles near the center elevation of each intraflow structure. The errorbars represent two standard deviations of the variation in the fracture angles. The large error bars are indicative of the scatter in the fracture angles.

The average fracture density in BH1 core is greatest in the upper colonnade and steadily decreases from there to the entablature and then to the lower colonnade. A zone of few fractures is still seen in the upper colonnade. Comparison of fracture densities in Figure 2.6 and fracture angles in Figure 2.7 with the photograph of outcrop shows that fracture characteristics in the subsurface (as measured on core) do not correspond well to what is expected based on outcrop. This finding supports the findings of previous researchers (cf., Long, 1978). The subtle shift to lower fractures in the lower colonnade also supports previous findings in Type III flows (Long and Davidson, 1981).

2.3.4 BH1 Core Crystal Textures

Petrographic descriptions of thin sections taken from BH1 core were made in a effort to determine the positions of intraflow structural contacts in the subsurface. As with

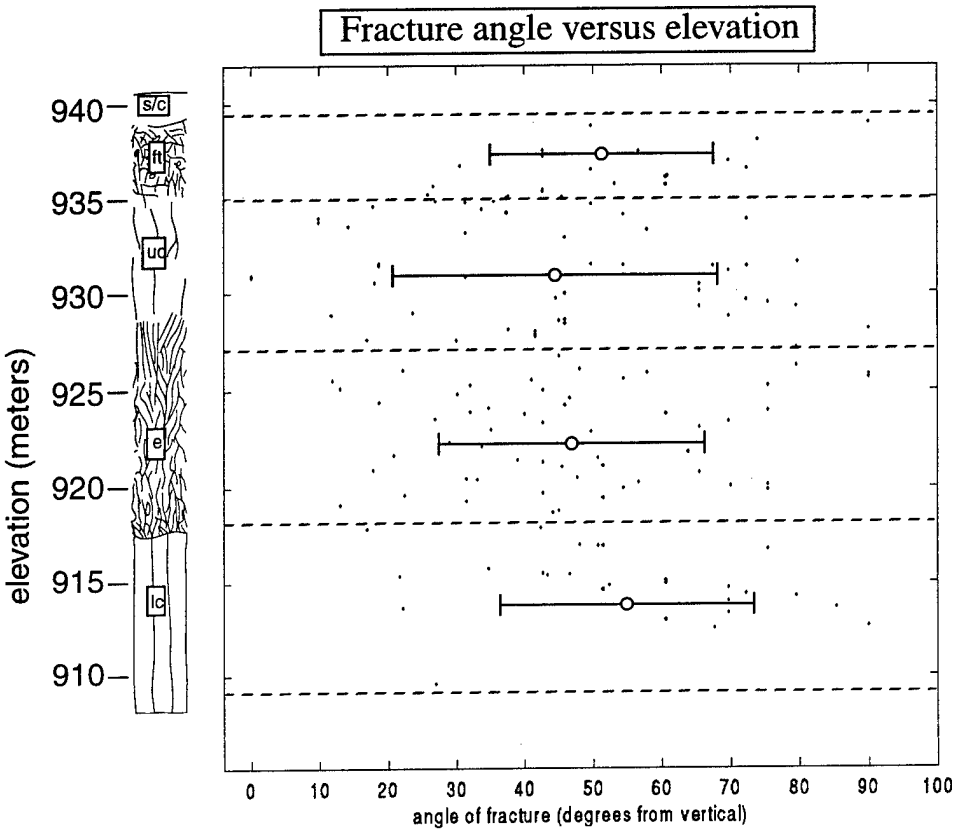

Figure 2.7 Fracture angle versus elevation for BH1 core. Plotted are the angles from vertical of all fractures, excluding driller's breaks. Fracture angles were calculated from measurements of either the greatest distance across the fracture face, or the distance of the fracture along the core. The precision of this measurement (+/- 0.0005m) is responsible for the vertical grouping of fracture angles that becomes more pronounced at higher angles. The mean fracture angle, and two standard deviations of it, are plotted near the central elevation for each intraflow structure.

differences in cooling fracture patterns, textural differences within lava flows are dependent on cooling rates. Petrographic studies by Long and Wood (1986) found that entablature has a higher abundance of glassy mesostasis than colonnade, which they attributed to quenching of the entablature during cooling. Degraff et al. (1989) studied the textures of several basalt flows, including the basalt of Lucky Peak, and found that

entablature consistently has more glassy mesostasis and a smaller average crystal size than lower colonnade. It is therefore expected that thin sections from BH1 core will show more glass in the entablature than the colonnades.

2.3.5 Petrographic Descriptions

Thin sections were made from BH1 core approximately every 1.5 meter along its length. Finished sections were approximately 25 millimeters (mm) by 20 mm. 500 points were counted in a grid with 1 mm node spacing. Five categories were distinguished according to the criteria below.

category:	plane polarized light:	cross polarized light:
1) glassy groundmass	amorphous groundmass, brown to black	isotropic
2) oxides	octahedral to subocta-hedral shape, black	opaque
3) phenocrysts	significantly larger than surrounding crystals (>10x)	
4) crystallized groundmass (other than oxides)	crystalline structure	anisotropic
5) vesicle/voids	groundmass missing from section; colorless	isotropic

Figure 2.8 shows plots of the glass, opaque, and crystal groundmass as a function of elevation in BLP. Percent composition is an aerial value based on the number of point counts in thin section, and can be taken to represent percent volumetric composition, known as the mode. Crystal groundmass is the sum of categories 2 and 4 above. Evident in Figure 2.8 is the inverse relationship of glass to crystal groundmass at each elevation. Glass is generally most abundant in the entablature, where it has an average modal

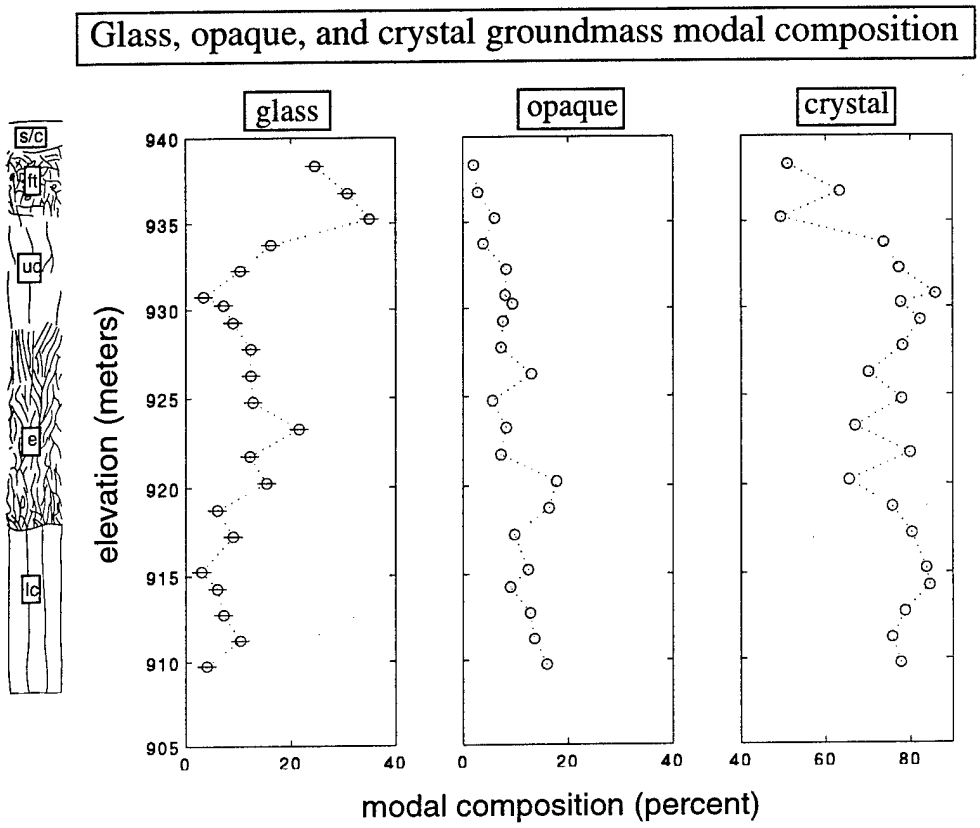

Figure 2.8 Glass, opaque, and crystal groundmass modal composition as a function of elevation in the basalt of Lucky Peak. Crystal groundmass includes all crystals other than phenocrysts (see text). On average, glassy groundmass is higher, and crystallized groundmass is lower, in the entablature than in the upper or lower colonnade. There is a subtle trend to lower composition of opaques at higher elevations in the flow. Error bars represent 95% confidence intervals; where no error bar is shown the error is less than the size of the plotted symbol.

proportion of 13.4%. Glassy groundmass averages 6.6% and 9.7% modal proportion in the lower and upper colonnades respectively. Crystallized groundmass averages 92.4%, 84.3%, and 86.6% modal proportion in the lower colonnade, entablature, and upper colonnade respectively.

The modal composition of opaque minerals, all of which are assumed to be Fe-Ti oxides, is also plotted in Figure 2.8. Near the top of the flow, the concentration of opaques in the mode decreases as the amount of glass increases. This can be explained in terms of quenching of the flow. As the magma cools, the melt becomes enriched in iron. If the flow is cooled rapidly past the precipitation temperature of iron oxides, the Fe-rich melt becomes glass before the oxides can crystallize. In general, therefore, the glass and iron oxide modal compositions should mirror each other, which is seen in Figure 2.8.

Phenocryst modal composition varies from 0 to 1.2 percent through the flow. No clear pattern is evident in the distribution of phenocrysts. The modal composition of vesicles and voids varies from 0 to ~9% through most of the flow, it is ~22% at 938 m elevation. Vesicularity is known to show consistent patterns in basalt flows, and high concentrations of vesicles will certainly affect physical properties of the flow. However, in this analysis, no distinction was made between "vesicles" inherent in the basalt, and "voids" caused by plucking crystals from the thin section during grinding.

The data in Figure 2.8 are consistent with the results of Long and Wood (1986) and Degraff et al. (1989) in that they show an increased amount of glassy groundmass in the entablature relative to the lower colonnade. The upper colonnade also contains less glass, which is consistent with it having cooled slower than the entablature. These data suggest that intraflow structure can be determined by comparing the textures of thin sections from core.

2.3.6 BH1 Dielectric Constant Measurements

Dielectric permittivity, ε, is defined by a constitutive equation that relates electric field intensity, E, with the electric displacement, D, (Keller, 1987):

$$D = \varepsilon E \qquad \text{(EQ 1)}$$

While dielectric permittivity is a constitutive parameter of a material that affects electrical properties of that material, it is sometimes more useful to refer to *relative dielectric permittivity*, or the *dielectric constant*, of a material when discussing its dielectric properties. Relative dielectric permittivity, or the dielectric constant, of a material, k, is defined as the ratio of the material's dielectric permittivity, ε, to the dielectric permittivity of free space, ε_o, (Ward, 1967):

$$k = \frac{\varepsilon}{\varepsilon_o} \qquad \text{(EQ 2)}$$

Dielectric constant measurements were made on hand samples taken from BH1 core to compare with radar propagation parameters. Radar propagation velocity in low conductivity formations is controlled primarily by dielectric permittivity, assuming negligible magnetic susceptibility (Ward, 1967). In the subsurface, the effective dielectric permittivity will be a composite of several features that are not present in hand samples, such as intervening soil and surface materials or interstitial moisture and infilling in the formation. However, changes in hand sample dielectric permittivity may show differences based on position in flow. These inherent differences in dielectric permittivity in the flow may be seen to relate to differences in radar velocity. Crystal texture differences in thin

sections may also relate to differences in hand sample dielectric permittivity measurements.

Twenty hand samples were cut from BH1 core in discs 6 cm in diameter and ~1 cm thick. Samples were taken approximately every 1.5 m along core. Measurements of the dielectric constant and loss were made by Dr. Indira Chatterjee and Dana McPherson at the University of Nevada, Reno, Electrical Engineering Department. Each sample was measured in the frequency range of 200 megaHertz (MHz) to 20 gigaHertz (GHz) using a Hewlett-Packard HP 85070B high-temperature dielectric probe. Three to four separate measurements were made in different places on each sample. Literature supplied by the manufacturer gives the typical accuracy of the dielectric probe as +/- five percent.

In Figure 2.9 the measured dielectric constants at 500 MHz of the hand samples are plotted as a function of the elevation of the hand samples in the flow. Measured constants between 200 and 500 MHz showed wide variability which was attributed to being at the edge of the effective range of the instrument (Chatterjee, 1996, personal communication). Values measured at 500 MHz are the closest to the GPR frequencies that are reliable. The values plotted are the mean of the three or four measurements made on each hand sample. Error bars on the plot represent 95% confidence intervals based on the number and variation of measurements made on each sample.

Figure 2.9 shows the dielectric constant in the hand samples ranges from ~2 to 10. Large error bars on some values are indicative of the wide variation in measured permittivity at different places on the sample, and the low number of measurements per sample. Samples from the flow top are highly vesicular; the increased air content of the

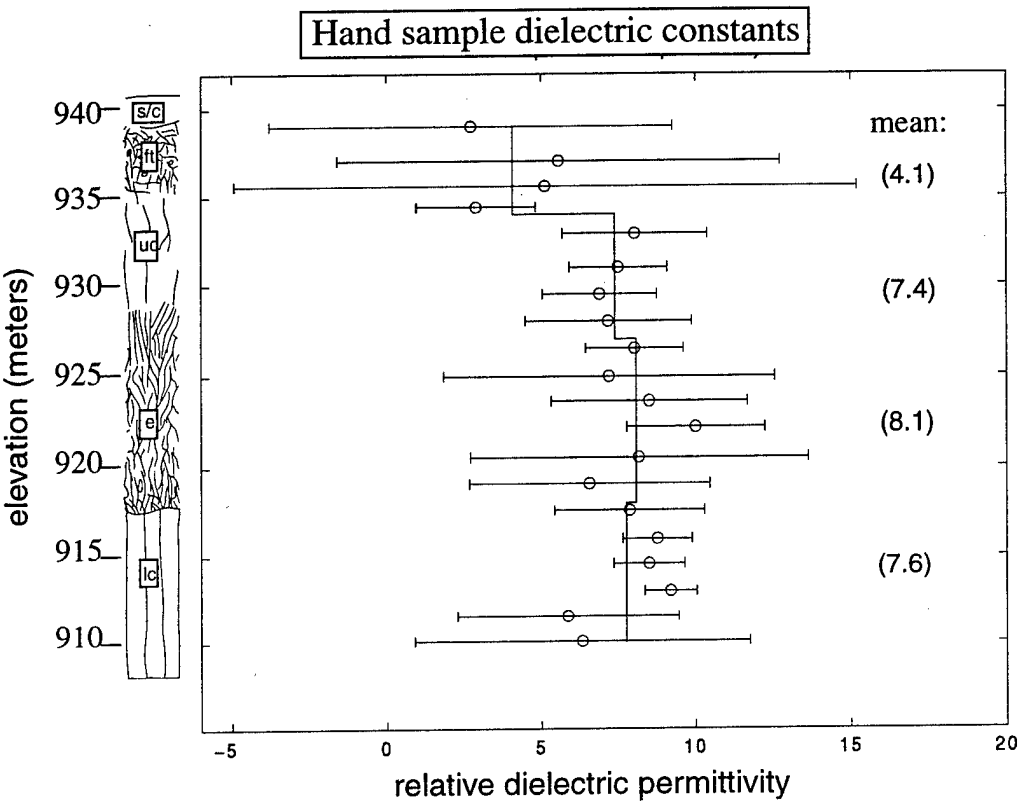

Figure 2.9 Relative dielectric permittivity (or, dielectric constant) of hand samples as a function of elevation. Plotted are the mean values of three or four separate dielectric constant measurements made on each hand sample. Error bars represent 95% confidence intervals based a Student's t distribution of the measurements per sample. Relative dielectric permittivity is seen to stay primarily between ~5 and 10. Lower relative permittivity near the top of the flow is attributed to the increased air content of the highly vesicular hand samples from this zone. The heterogeneous distribution of the vesicles also accounts for the large variations of measured values.

samples probably accounts for the lower overall relative permittivity in this zone. The heterogeneous distribution of this air also accounts for the wide variation in values from individual hand samples (Chatterjee, 1996, personal communication). The mean value of the dielectric constant in each intraflow structure is plotted as a line through the structure. The mean dielectric constant is slightly higher in the entablature than the upper or lower colonnade, and lowest in the flow top. However, the large error bars in the hand sample measurements do not allow for these changes to be called statistically significant.

2.4 Electromagnetic Data

2.4.1 Resistivity of the Subsurface

Bulk electrical resistivity soundings of the subsurface were performed using Schlumberger resistivity and time domain electromagnetic (TDEM) methods. Detailed descriptions of these methods are given by Ward (1990). In this thesis, a brief summary of the principles involved with each method will be given along with the results. In a Schlumberger resistivity sounding, a current is injected into the ground between two electrodes and a voltage is measured between two other electrodes. The voltage difference between the receiver electrodes is a function of the distances between the electrodes, the injected current, and the resistivity of the subsurface (Ward, 1990). Since the first two of these factors are known, the measured voltage difference can be used to determine the apparent resistivity of the subsurface. An automated data processing software package from the USGS was used to invert apparent resistivity data to a resistivity-depth profile (Zohdy and Bisdorf, 1989).

In TDEM soundings, a current put through a wire coil laid on the ground surface creates a magnetic field around the coil and a secondary magnetic field in the earth (McNeill, 1990). When the current is turned off, the primary magnetic field (from the transmitter coil) is extinguished, and the secondary (or transient) magnetic field in the earth begins to decay. The decay of the transient field is measured by the voltage it creates in a receiver coil. A smooth, exponential decay of the secondary magnetic field is expected for an infinitely resistive, homogeneous half-space. Variations in the conductivity of the subsurface cause deviations from exponential decay. Such deviations result from eddy currents created in conductive bodies in the earth by the collapsing primary field. These currents decay with time and produce deviations in the decay of the transient field (McNeill, 1990). Automated software packages can be used to forward- or inverse-model the data based on known geology (Interpex, 1996).

2.4.2 Schlumberger and TDEM Data Acquisition

Schlumberger resistivity data were collected using a Zonge GDP-16 multifunction receiver. An electrode array was placed along a line perpendicular to and centered on the axis line of the study site (Figure 2.3). Receiver electrodes (m and n) were placed 0.5 m on either side of the center of this line. Transmitter electrodes (A and B) were placed 1 m on either side of the center for the first reading. The distance between the transmitter electrodes and the center was then doubled for each successive reading out to a distance of 128 m. Transmitter current, I, was 0.1 amp and transmitter frequency was 0.125 Hz (8 second period). Voltage, V, between the receiver electrodes is measured by the receiver and apparent resistivity, ρ_a, is then given by:

$$\rho_a = \pi \times \frac{V}{I} \times \left(\frac{a^2}{b} - \frac{b}{4}\right) \qquad \text{(EQ 3)}$$

where: a = one half the distance between electrodes A and B (i.e., AB/2)

b = distance between electrodes m and n.

Data were processed using USGS software for processing Schlumberger sounding curves (Zohdy and Bisdorf, 1989). This software uses an ordinary least squares algorithm to fit a smooth curve to the data, and if the error between the data and curve is less than 2%, a model the of resistivity versus depth is created from the smooth curve (Zohdy and Bisdorf, 1989).

Figure 2.10 shows the smoothed curve and interpreted model of the Schlumberger resistivity data collected in the study area. The model shows three layers: a thin surface layer with resistivity ~100 ohm-meters and a thickness less than 1 m; a middle layer with a resistivity of 30 ohm-meters and a thickness of ~2 m; and a bottom layer of resistivity ~1800 ohm-meters. The bottom layer is essentially a homogeneous half space extending to infinity in the model. This bottom layer is interpreted as the basalt. Transmitter electrode spacing was not great enough to get resistivity information from beneath the basalt.

TDEM data were collected using a Zonge GDP-16 multifunction receiver and a Zonge Nanotem transmitter at a point near the center of the well filed (Figure 2.3). A 400 m^2 (20 x 20 m) coil loop was placed on the ground and connected to the transmitter. The receiver loop was 4 m^2 (2 x 2 m) and placed inside the transmitter loop. Transmitter current was 3 amps, the transmitter frequency was 32 Hz. Voltage in the receiver loop was

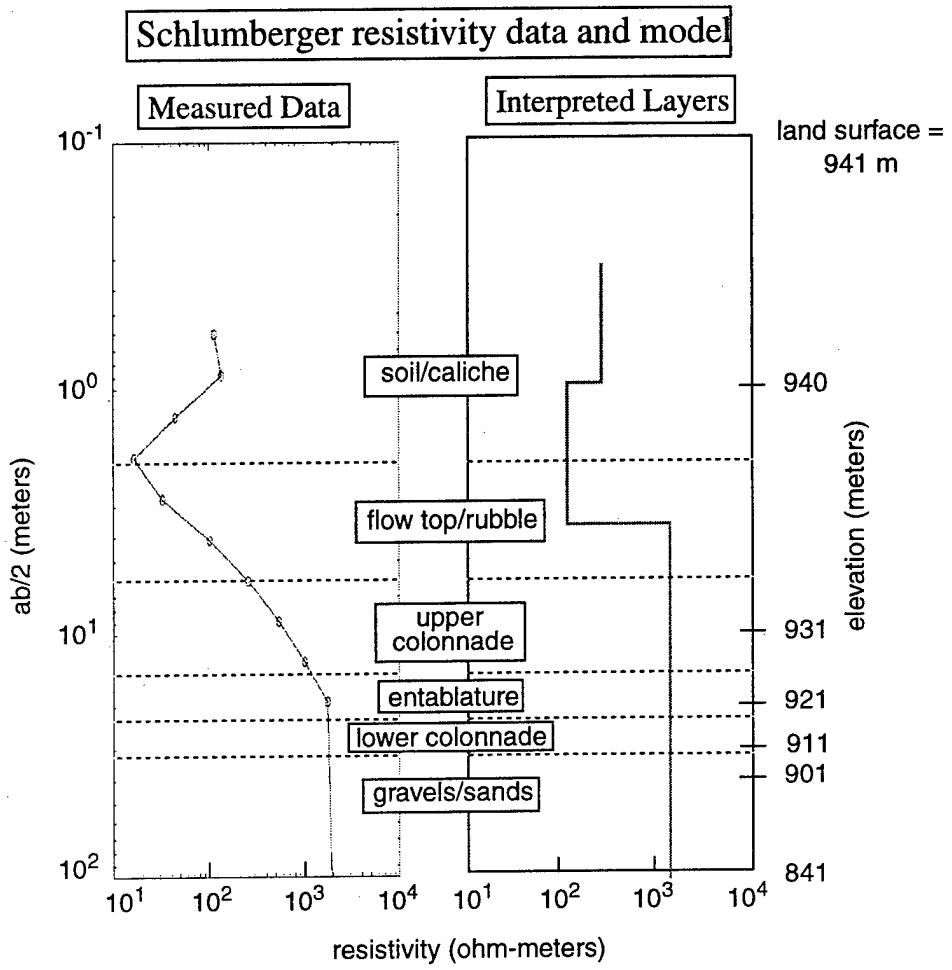

Figure 2.10 Schlumberger resistivity data and inversion model. Field data are plotted as function of ab/2 (see Figure 2.3). The interpreted layer resistivities are plotted as a function of elevation. The interpreted model shows a shallow, moderate resistivity surface layer, over a higher resistivity homogeneous half space. This model correlates well with a soil-caliche layer over the basalt flow.

measured at a logarithmically increasing sample rate in each sounding. Data were reformatted for processing using proprietary software of Zonge, and then interpreted using automated software from Interpex, Inc. This software uses a ridge-regression technique to fit a model to the calculated data (Interpex, 1996).

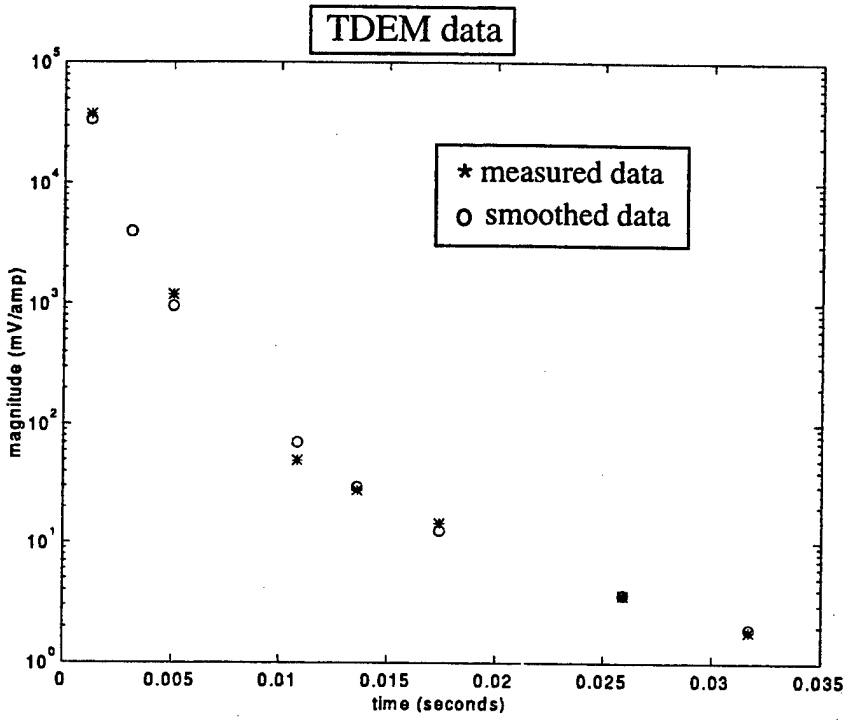

Figure 2.11 TDEM data. Plotted are the measured data of the transient electromagnetic field decay and the smoothed data generated by the interpretation software. These data show a nearly exponential decay in the transient field.

Figure 2.11 is a plot of the measured and smoothed TDEM data. The measured data show a smooth decay in the transient magnetic field that appears nearly exponential. Figure 2.12 is a plot of an inversion model generated by the Interpex software using the smoothed data. In the figure, resistivity is plotted as a function of elevation. The dashed data lines are the resistivities versus depth for three separate inversions, the solid data line is the mean resistivity from the three separate inversions for each layer. The horizontal dashed lines represent the known elevations of lithologic boundaries between the basalt

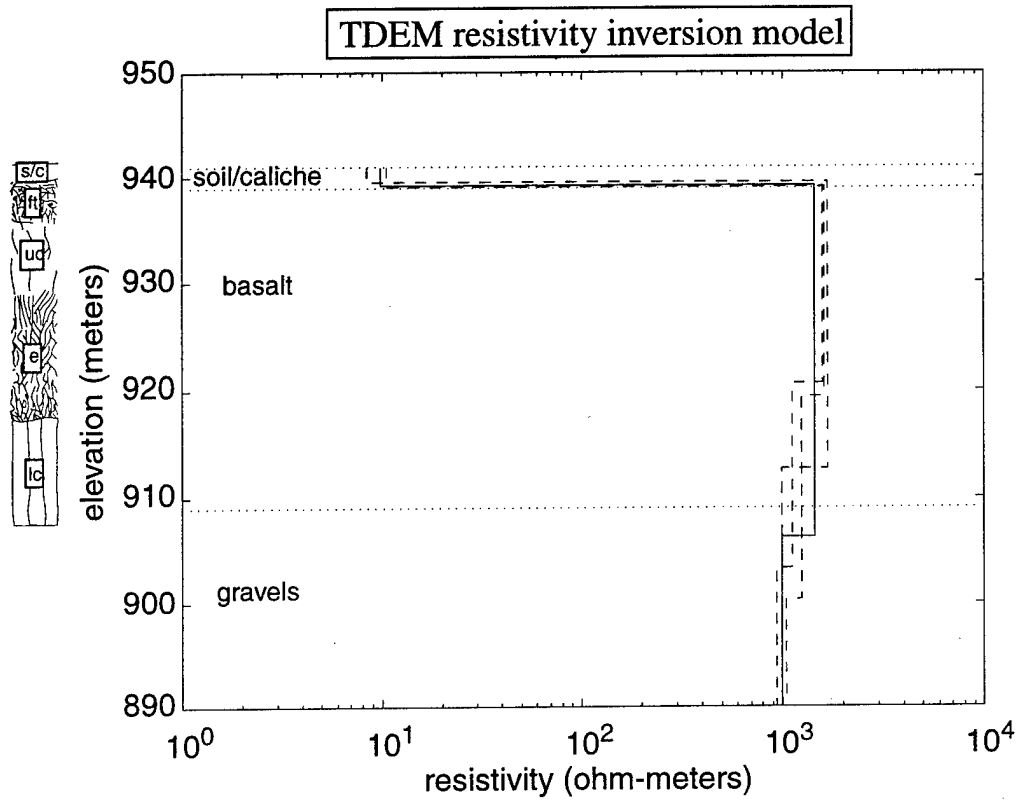

Figure 2.12 TDEM resistivity inversion model. The dashed lines represent three separate inversion models generated by the Interpex TDEM inversion software, with individual errors of 18.2, 19.1, and 19.3%. The solid line is the mean of the resistivities given for each layer by the separate models. A stylized geologic column is included for reference. The models show a thin, low resistivity surface layer over a more resistive, deeper layer.

and adjacent units. The model shows a ~10 ohm-meter surface layer over a ~1800 ohm-meter layer with a thickness of approximately 30 meters. A homogeneous half space with a resistivity of ~1000 ohm-meters comprises the bottom layer in the model. Each inversion in this model used seven data points in the transient field decay curve. The starting models of each inversion varied from one another in the thickness of the basalt layer. The errors of the three inversion models were 18.2, 19.1, and 19.3% between the

calculated model and the real data. Other models with approximately the same error were generated, however, they either did not fit the known geology well, or consisted of more layers and thicknesses than the small number of data points warranted.

2.4.3 Discussion of Resistivity Soundings

Figure 2.10 and Figure 2.12 show the resistivity versus depth in the study area derived from two separate sources. Inspection of these figures show that the interpreted layers and resistivities are in close agreement. The composite model is a low resistivity (~10-20 ohm-meter) surface layer with a higher resistivity (~1800 ohm-meter) layer beginning at approximately 2 meters depth. The resistivity of the surface layer is lower than might be expected for normal soils. This might be explained by saline water in the extreme near surface. The resistivity of the basalt is reasonable for a dry, hard rock layer. The layer thicknesses in this model agree well with the known geology of the study area.

Information from below the basalt is difficult to obtain from Schlumberger soundings primarily because of the proximity of the cliff. Any electrode spacing great enough to image below the basalt would also measure effects from the void beyond the cliff. Resolution in TDEM data is also hampered by the particulars of this site. Basalt has very low conductivity (high resistivity), and therefore does not generate a significant transient field. This limits the number of samples of usable data before noise swamps the signal, thus limiting the number of free parameters that can be reliably inverted from the data.

Neither the Schlumberger, nor the TDEM data, indicate changes in resistivity within the basalt flow. Such changes, if present, could be used to explain radar velocity and

attenuation results discussed later in this thesis. It is possible that these changes exist and that the surface methods used were not capable of distinguishing them. The low resolution of the methods cannot rule out the presence of, nor confirm the lack of, a resistivity change within the flow.

3. SEISMIC DATA

3.1 Introduction

3.1.1 Review of Seismic Wave Propagation

Seismic wave velocity in geologic material is a function of the elastic moduli of the material. Seismic wave attenuation in geologic material is related to the inelastic properties of the material (Dyck and Young, 1985). It is therefore possible to use seismic velocity and attenuation measurements to gather information on the elastic and inelastic properties of the subsurface. Dyck and Young (1985) present data to show that increased fracture density in a formation causes a decrease in compressional wave velocity. Increased fracture density also increases attenuation of the higher frequencies in the received wave form (Dyck and Young, 1985). Fracture density and orientation appear to change dramatically in outcrop of the basalt of Lucky Peak; fracture density measured on core changes slightly between intraflow structures. It was expected that this change will be detected as changes in the velocity and attenuation of the seismic waves.

Velocity analysis of seismic data involves measuring the travel times of seismic waves over selected intervals. If Δd is the difference in travel distance of a seismic wave over some interval in the subsurface, and Δt is the difference in travel time of the wave from the start to end of the same interval, then the average interval velocity, v, of the wave is given by:

$$v = \Delta d/\Delta t. \qquad \text{(EQ 4)}$$

Velocity is thus shown to be the slope of a travel distance versus travel time plot.

Kudo and Shima (1970) give a method of determining seismic attenuation as a function of frequency. They show that attenuation can be calculated by comparing the amplitude spectra of two seismic waves that have traveled different distances in the subsurface. In the analysis presented here, phase information in the amplitude spectra caused by differences in arrival time is removed by using the square root of the spectrum of the autocorrelation of the waveform. Assuming spherical divergence and exponential decay of the seismic wave, the attenuation coefficient, $\alpha(f)$, in decibels per meter (dB/m), is given by:

$$\alpha(f) = -(8.686) \times \frac{1}{R_i - R_j} \times ln\left(\frac{R_i A_i(f)}{R_j A_j(f)}\right) \qquad \text{(EQ 5)}$$

where:

R_i = distance wave traveled to receiver i

R_j = distance wave traveled to receiver j

$A_i(f)$ = square root of spectrum of autocorrelation of trace i

$A_j(f)$ = square root of spectrum of autocorrelation of trace j

3.2 Acquisition

3.2.1 BH1 Vertical Seismic Profiles

A vertical seismic profile (VSP) experiment was conducted in BH1. Figure 3.1 shows the configuration of the experiment. The source location was 1.35 meters (m) south of the borehole. Both S- and P-wave sources where used at this location. A three component reference geophone was located on the surface, approximately symmetrically across the borehole from the source. A three component, side wall clamping, downhole geophone

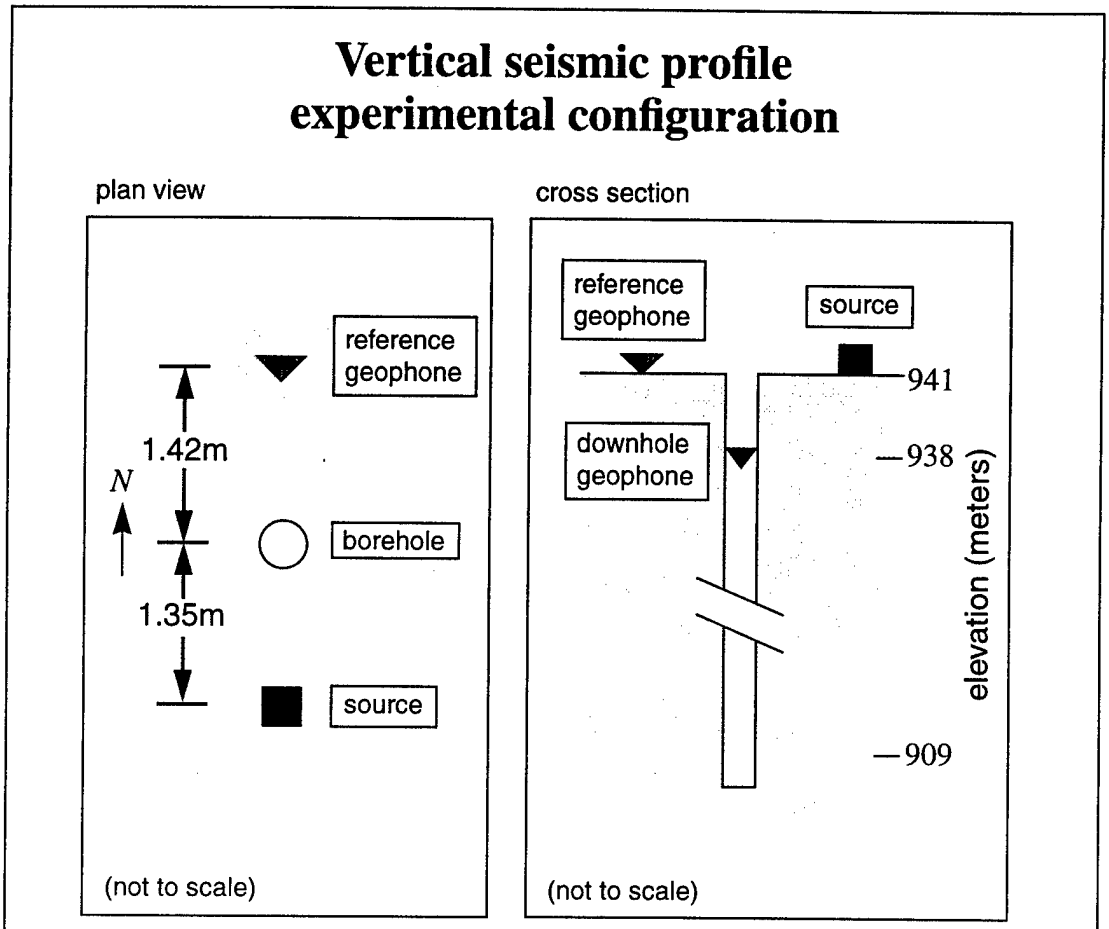

Figure 3.1 Vertical seismic profile experimental configuration. The experiment was conducted in BH1 (Figure 2.3). The source location was 1.35 m south of the borehole, a three component reference phone was located on the surface 1.42 m north of the borehole. A three-component side-wall clamping downhole geophone was used in the borehole. For each source run, the borehole geophone was started at the bottom of the borehole (909 m elevation), and then moved in one meter increments up the borehole to three meters below land surface (938 m elevation).

was used in the borehole. Each source run began with the downhole geophone at the lowest elevation (909 m above sea level). Successive records in each run were then made at one meter intervals up the borehole to the highest elevation (938 m above sea level).

The S-wave source was a 1.2 m long railroad tie that was laid perpendicular to the line between the source and borehole and loaded on top with sand bags. Sledge hammers were mounted on pivots on each end of the tie in such a manner that the hammers could swing in a repeatable manner to strike the ends of the tie, generating the S-waves. Records were made with both polarities of the source at each level before moving to the next level. During the S-wave source run, the transverse component of the downhole geophone became inoperative. This occurred at an elevation of 925 m, and limited options for processing S-wave data above this elevation.

The P-wave source consisted of a sledge hammer mounted on a 1.2 m long board in such a manner that the hammer pivoted to strike the board in the vertical direction. This source was also weighted with sand bags. During P-wave data collection, the source became dislodged from its position on the surface, necessitating reseating. This "rearranging of the source" caused a change in the source spectrum that was evident in the reference phone data. Compensating for this change was required in later processing.

3.3 Processing

3.3.1 Seismic Velocity Analysis

A total of 90 seismic records were recorded--two S-wave source polarities (90° and 270° azimuth) and one P-wave at each of 30 levels. Six channels were recorded in each record, three each for the reference and downhole geophones. Individual channels from these records were combined to create files with P-wave, S-90°, or S-270° data from the downhole geophone and reference geophone. For velocity analysis, one S-wave polarity was subtracted from the other, effectively enhancing the S-wave arrivals. Figure 3.2 shows plots of the P-wave data and the subtracted S-wave data.

Velocity analysis of seismic data requires the picking of the first arrival in each trace. Noise in the records make picking the first motion of the arrival difficult. For this reason, the arrival of first peak in the wave form was picked. Figure 3.3 shows an example of this from the P-wave data. Use of this arrival assumes negligible change in the waveform between traces.

Figure 3.4 is a plot of the P-wave first peak arrivals versus elevation. The arrivals fall into two groups, with a break at 927 m elevation. Least squares, best fit lines have been fit to the data and are plotted in the figure. The slopes of these lines translate to velocities of 1060 m/s in the flow top and upper colonnade and 3390 m/s in the entablature and lower colonnade.

Figure 3.5 is a plot of the first peak arrivals from the subtracted S-wave data. As with the P-wave data in Figure 3.3, the arrivals fall into two groups with a break at 925 m elevation. A significant change in the received wave form precluded picking a consistent

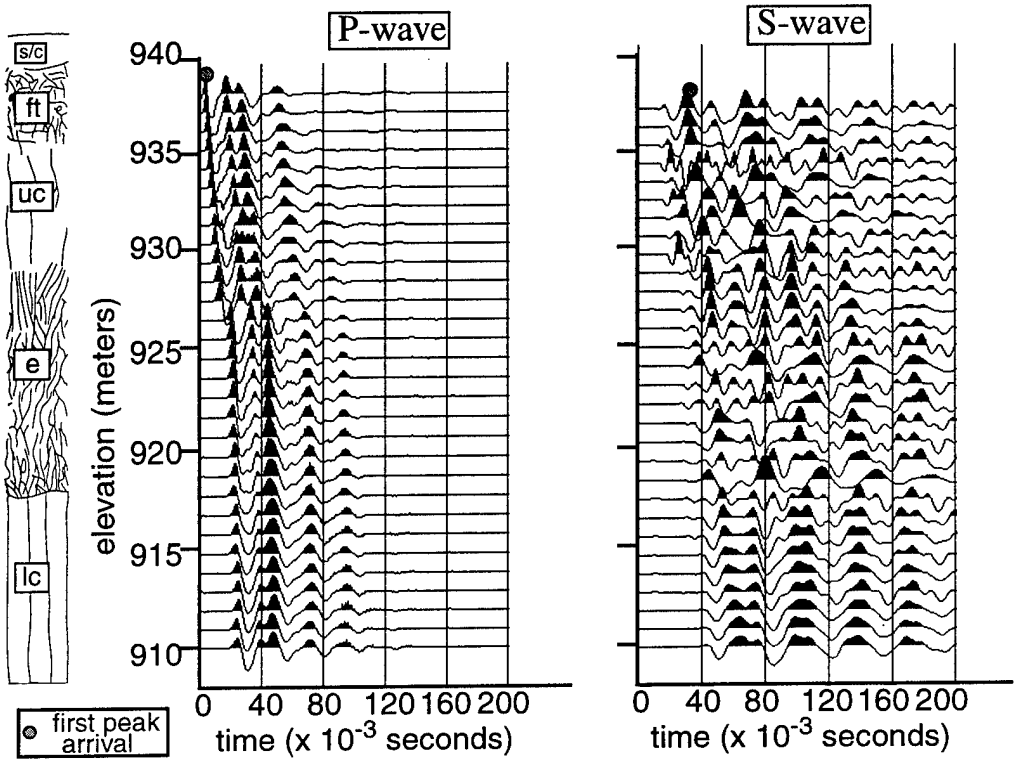

Figure 3.2 VSP data sets. P-wave data represents the vertical component of the downhole geophone with the P-wave source. The S-wave data is the result of subtracting the two polarities of the source from each other, and was low pass filtered (cutoff 100 Hz). A stylized geologic column is included for reference. An example of the first peak arrival is shown on each data record. This arrival was more easily picked than the first motion, and was used for velocity analysis (see Figure 3.3).

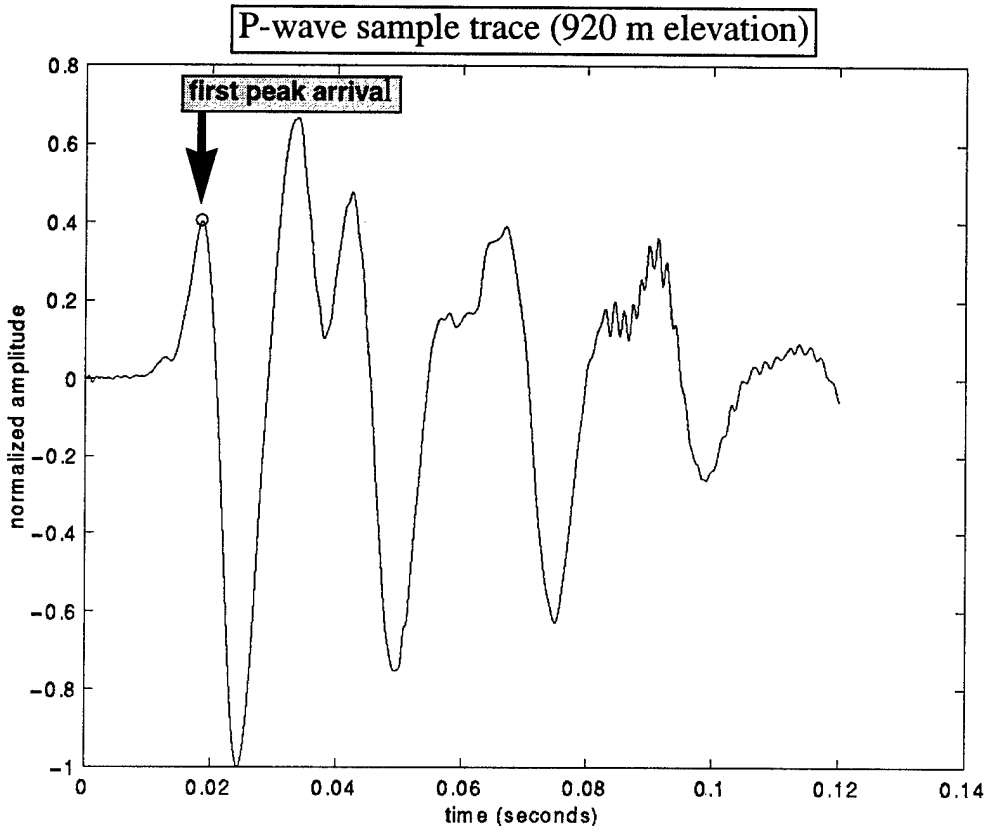

Figure 3.3 Sample trace from P-wave data. Plotted is trace 20 (920 m elevation) from the P-wave data. The first peak arrival was used in velocity analysis; its location in this trace is shown in the figure. The high frequency noise after ~0.08 seconds is interpreted as an air wave in the borehole.

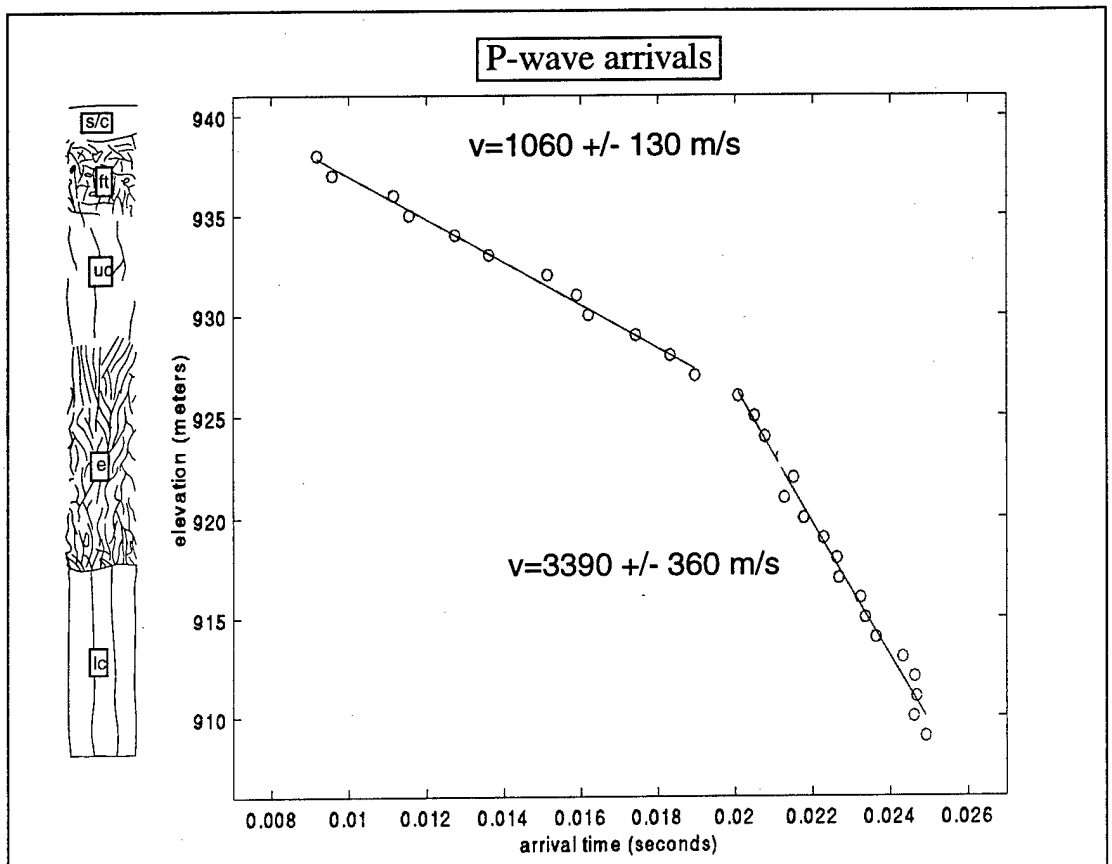

Figure 3.4 P-wave arrivals. Plotted are the first peak arrivals of the P-wave data as a function of elevation. Two groups of arrivals are clearly evident with the break between them at ~927 m elevation. Least squares best fit lines have been plotted over the arrivals. Velocities were calculated based on vertical travel distances.

arrival above and below approximately 925 m elevation. This explains the offset in arrival times at this level in Figure 3.5. Best fit lines to these arrival times indicate S-wave velocities of 600 m/s and 1700 m/s above and below 925 m, respectively.

3.3.2 Seismic Attenuation Calculations

Attenuation analysis of the seismic data was hampered by problems with data collection. As mentioned above, the transverse channel of the downhole geophone

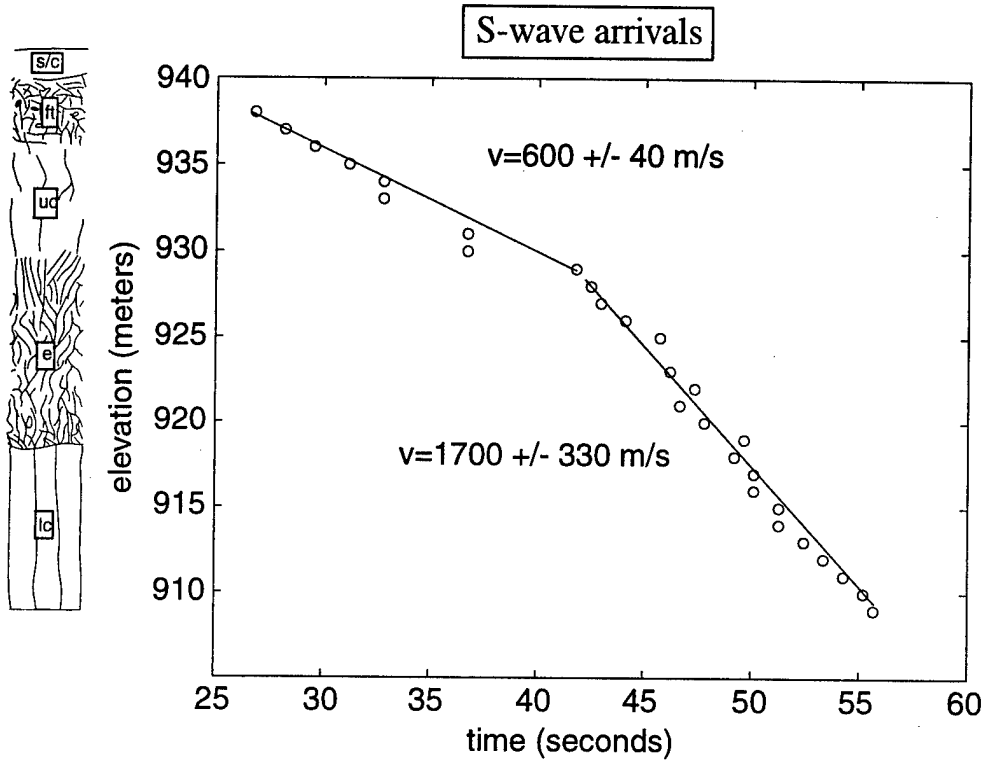

Figure 3.5 S-wave arrivals. Plotted are the first S-wave peak arrivals. Two groups can be seen in the arrivals with a break at ~926 m elevation. Least squares best fit lines plotted over the arrivals gives velocities of 600 m/s in the flow top and upper colonnade, and 1700 m/s in the entablature and lower colonnade

became inoperative during data collection. The lack of this channel in the data precludes rotating the two horizontal components of the S-wave data, which is necessary for complete spectral analysis. For this reason, attenuation calculations were not made with the S-wave data.

Spectral shaping of the P-wave data was necessary to compensate for the change in source spectrum during data collection. The principle of spectral shaping is to use the reference phone data to determine how the source changed during the experiment. The

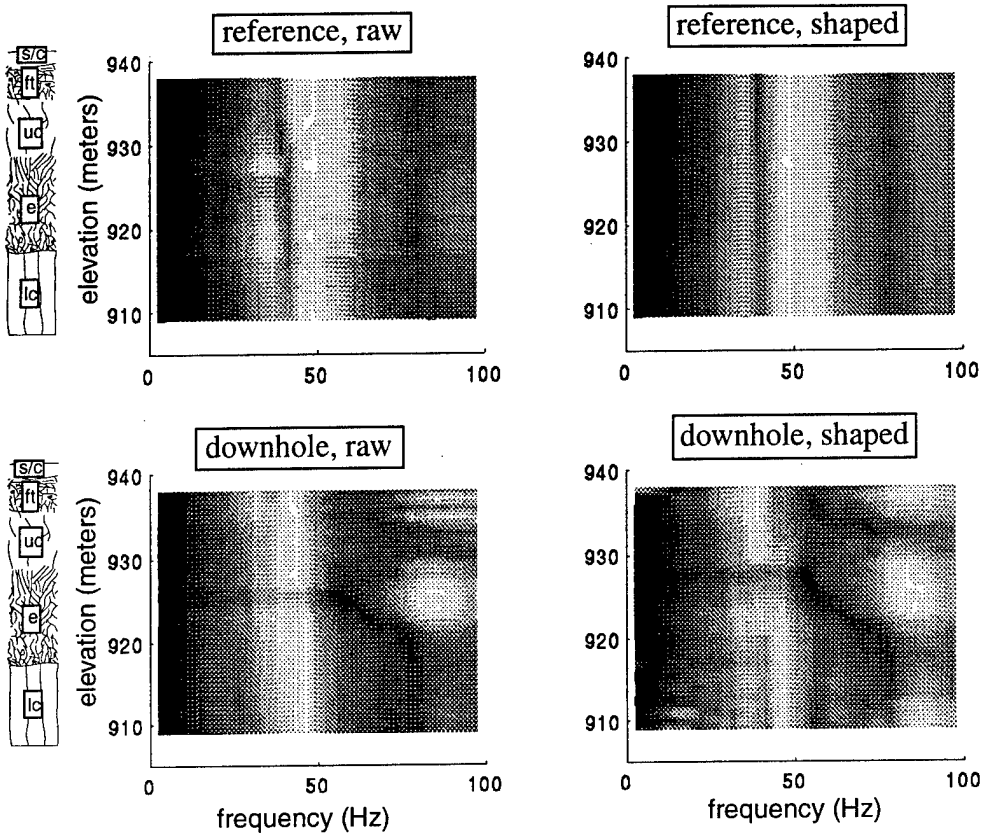

Figure 3.6 Seismic P-wave amplitude spectra before and after shaping. Spectral shaping was required to remove the effects of source spectrum changes during the experiment. Plotted are the amplitude spectra of the raw and shaped reference and downhole geophone data. Trace 17 (921 m elevation) was used as the target trace for shaping the reference data. The filters required to match each trace with the target were then applied to the respective downhole traces. The shaped downhole data can then be used for further spectral analysis.

amplitude spectrum of the vertical component of the reference phone is plotted in the upper left of Figure 3.6. Inspection of this plot shows the received spectrum does change from trace to trace (note that elevation in the reference phone plots refers to the elevation of the downhole geophone for the respective reference trace). Since the reference phone was not changed during the experiment, the change in received spectrum is attributed to a change in source spectrum.

In order to accomplish spectral shaping, a "target trace" is chosen in the reference phone data. A Weiner least squares filter is then designed for each of the other reference traces to bring their spectra as close as possible to the target trace's spectrum. These individual filters are then applied to the respective downhole data traces, effectively removing changes in source spectrum during the experiment. Plotted in the upper left of Figure 3.6 is the reference data after shaping. The spectra of the "raw" and "shaped" downhole data are plotted in the lower left and lower right of Figure 3.6, respectively. These shaped data are then used for further processing.

In order to choose the best target trace in the reference phone data, an objective function was defined as the sum squared error of the difference, in the time domain, between the target trace and each shaped trace. If the result of the shaping routine were perfect, the shaped traces would be identical, and the value of this objective function would be zero. The higher the value of this function, the less effective was the shaping routine at removing the changes in the source spectrum. To determine the best target for shaping, the objective function was evaluated for six different traces spaced regularly

throughout the data. The trace that minimized this objective function, trace 17, was chosen as the target.

After spectral shaping, the P-wave data was used to calculate attenuation by the spectral ratio method described above (Equation 5). Attenuation in each intraflow structure was calculated by comparing the amplitudes of traces recorded four meters above and below the center of the structure. The centers of the structures were taken to be 913, 922, 932 meters elevation for the lower colonnade, entablature, and upper colonnade respectively. Figure 3.7 shows plots of the attenuation coefficient, α, plotted as a function of frequency for each intraflow structure. Inspection of the plots reveals α to be highest in the upper colonnade, moderate in the entablature and lowest in the lower colonnade. Also evident in the plots is a very low variation of α with frequency. Error bars in these plots account for the variation in measured amplitude for five traces centered on the middle of each intraflow structure.

Figure 3.8 is a plot of the attenuation coefficient, α, plotted as a function of elevation. For this plot, α was calculated using the ratio of amplitudes from traces eight meters apart and plotted at the center of a sliding window. The value of α plotted is the mean for 20 frequencies between approximately 23 and 73 Hertz (Hz). Error bars represent two standard deviations of the variation in α over those 20 frequencies. Figure 3.8 confirms what is seen in Figure 3.7, that is, attenuation of approximately 7 dB/m in the upper colonnade, 5 dB/m in the entablature, and 2 dB/m in the lower colonnade.

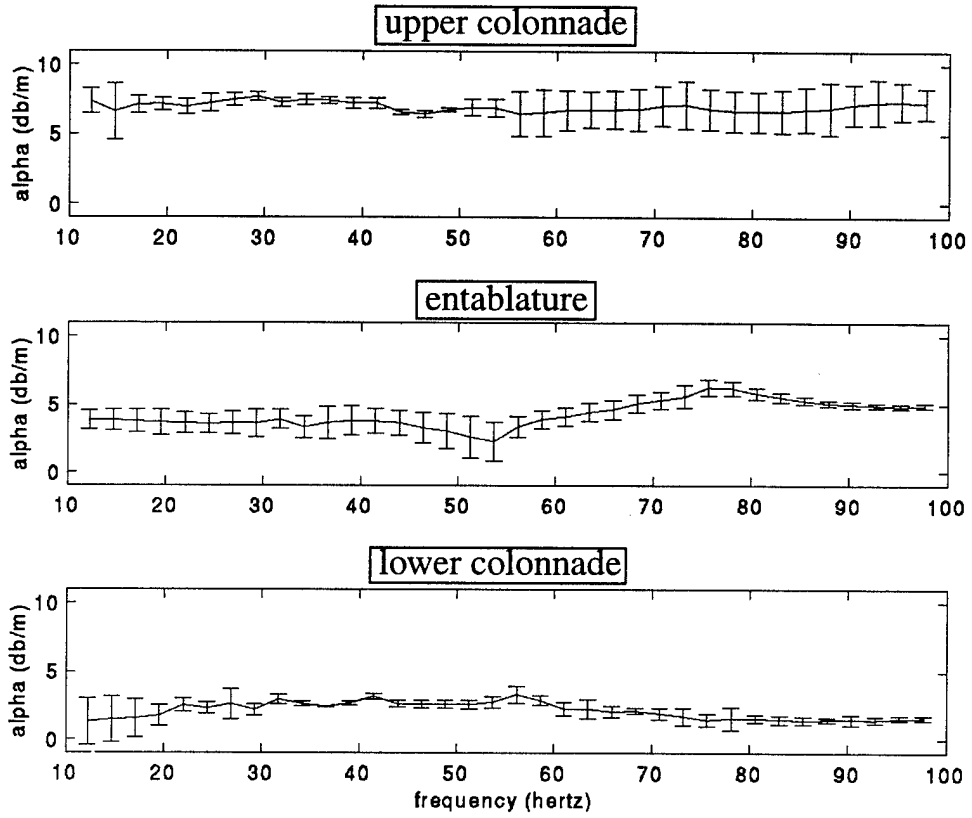

Figure 3.7 Seismic P-wave attenuation as a function of frequency for intraflow structures. Plotted is the calculated attenuation (α), in dB/m, in the frequency range of approximately 12-98 Hz, for the center of each intraflow structure. Attenuation was calculated by spectral ratio over an 8 meter distance in elevation. Attenuation is seen to vary only slightly over the plotted frequency range in each structure, which is contrary to the expected increase in attenuation with increasing frequency. Error bars in the plots are 95% confidence intervals based on the variations in the amplitude spectra of five traces centered on the middle of each intraflow structure.

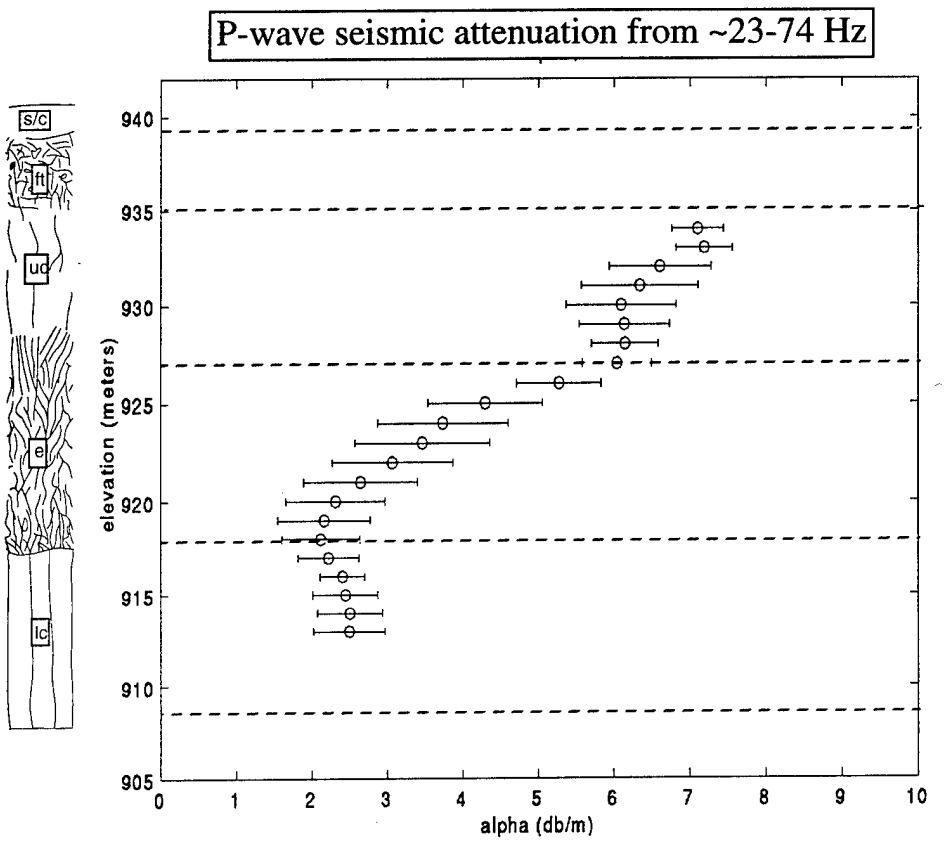

Figure 3.8 Mean P-wave seismic attenuation for the frequency range of 23-74 Hz as a function of elevation. P-wave seismic attenuation (α) was calculated by spectral ratio as a function of frequency over a sliding 8 m window. The mean value of α over the frequency range ~23-74 Hz was calculated and plotted at the center of each window position. Attenuation is greatest at the top of the flow, where the flow top rubble zone influences the calculation of α. Attenuation is significantly lower in the entablature and lower colonnade compared to the upper colonnade and flow top. Error bars in the plot are 95% confidence intervals based on the variation in α over the frequency range of interest at each elevation.

3.4 Interpretation

3.4.1 Correlation of Seismic Results with Geology

Both P- and S-wave velocities increased below ~926 meters elevation (the upper colonnade-entablature boundary). This result suggests an increase in formation stiffness at this elevation, which correlates with fracture measurements in core. Fracture counts on BH1 core showed a decrease in fracture density in the entablature compared to the upper colonnade (Figure 2.6), and might explain the increased velocity and decreased attenuation in the entablature compared to the upper colonnade. No clear break in velocity is seen between the entablature and lower colonnade. A clear decrease in P-wave attenuation is seen between the upper colonnade and entablature (Figure 3.8). P-wave attenuation declines steadily through the entablature and is lowest at the entablature-lower colonnade boundary. Attenuation is lower in the lower colonnade compared to the upper colonnade. This attenuation pattern correlates with the a general decrease in fracture density from the upper colonnade through the entablature to the lower colonnade in BH1 core. Attenuation of P-wave seismic energy was shown not to be strongly frequency dependent.

The seismic results presented here do not correspond to what is expected based on outcrop. Because of the obvious increased fracture density in the entablature compared to the upper and lower colonnade seen in outcrop, it was expected that the entablature would show decreased velocity and increased attenuation compared to the other structures. This may be explained by the general lack of correlation between outcrop and core fracture characteristics (see section 2.3.2). However, the measured fracture densities on BH1 core

do not explain all the results presented here. The lower colonnade has comparable lower fracture density compared to the entablature as the entablature does to the upper colonnade, yet no increase in velocity is seen between the lower colonnade and entablature. It is possible that weathering is affecting the seismic velocities. Weathering decreases rock competence, and thus decreases seismic velocities. The upper portion of the flow would be expected to be more weathered than lower sections, and the low velocity in the upper colonnade compared to the rest of the flow might thus be indicative of increased weathering.

4. RADAR DATA

4.1 Introduction

4.1.1 Review of Radar Wave Propagation

Ground penetrating radar (GPR) uses megahertz frequency electromagnetic radiation to probe the earth. Ward (1967) derives equations to calculate the attenuation and velocity of electromagnetic waves in geologic material from generalized wave equations solved in one dimension. The amplitude of the electrical and magnetic field as a function of time and position are given by:

$$E = E_0 \exp i(\omega t - kx) \quad \text{(EQ 6)}$$

$$H = H_0 \exp i(\omega t - kx) \quad \text{(EQ 7)}$$

where the complex wave number, k, is given by:

$$k = \beta + i\alpha. \quad \text{(EQ 8)}$$

Parameter β and α are the real and imaginary parts of the wave number, respectively, and are given by:

$$\beta = \omega \times \sqrt{\frac{\mu\varepsilon}{2}} \times \left[\left(1 + \frac{\sigma^2}{\varepsilon^2 \omega^2} \right)^{0.5} + 1 \right]^{0.5} \quad \text{(EQ 9)}$$

$$\alpha = \omega \times \sqrt{\frac{\mu\varepsilon}{2}} \times \left[\left(1 + \frac{\sigma^2}{\varepsilon^2 \omega^2} \right)^{0.5} - 1 \right]^{0.5} \quad \text{(EQ 10)}$$

where ω = angular frequency of electromagnetic wave

σ = direct current electrical conductivity of the medium

ε = dielectric permittivity of the medium

μ = magnetic permeability of the medium

The phase velocity, v, of a radar wave propagating through a geologic medium is given by:

$$v = \sqrt{\frac{2}{\mu\varepsilon}} \times \left[\left(1 + \frac{\sigma^2}{\varepsilon^2 \omega^2} \right)^{0.5} + 1 \right]^{(-0.5)} \qquad \text{(EQ 11)}$$

The attenuation and velocity of radar waves in geologic materials is thus shown to vary by the frequency of the waves, and is dependent on the electromagnetic constituent parameters of the geologic material. When these constitutive parameters change across lithologic boundaries, the radar wave propagation characteristics will also change. Constituent parameters may change because of petrographic differences in the rock, because of changes in the heterogeneities in the rock matrix, or because of the presence of water or infilling materials. GPR will respond to changes in the effective, bulk constitutive properties of the media between the antennas.

4.1.2 Expected Behavior of Radar in Basalt

Electrical conductivity is inherently low in dry basalt (Touloukian, 1989). Basalt has a high iron content which results in a correspondingly high magnetic permeability (CRC, 1989). The dielectric constant of dry basalt at radar frequencies is ~10^1, which is similar to other dry geologic media (CRC, 1989). These properties suggest radar waves, in general, should propagate through basalt with relatively high velocity and low attenuation.

An expected velocity and attenuation of radar waves in basalt can be calculated using Equations 10 and 11. Using the mean dielectric constant of 7.7 measured on BLP hand samples (Figure 2.9), the calculated electrical resistivity of 1800 ohm-meters for the BLP formation (Figure 2.10 and Figure 2.12), an estimated relative magnetic permeability of 1.18 for basalt (CRC, 1989), and a radar frequency of 60 MHZ, the expected velocity of a radar wave is 9.94×10^7 meters/second. Using the same values (and modifying Equation 10 to calculate attenuation in dB/m), the expected attenuation of the radar wave is -0.07 dB/meter. These estimated values for velocity and attenuation are based a combination of a bulk resistivity measurement, hand sample permittivity measurements, and an estimated permeability value. Therefore, they should be taken as "gross estimates" only.

Two physical properties in basalt flows change at the upper and lower entablature boundaries. In outcrop, the most visible change is fracture density and orientation; fracture density is greater, and orientation more random, in the entablature than in either the upper or lower colonnade (Figure 2.5). Evidence for this change in fracture characteristics at intraflow boundaries in the subsurface is equivocal (Long and Davidson, 1981). BH1 core fracture measurements show some variation in fracture densities at intraflow structural boundaries (Figure 2.6). Olhoeft (1990) states that inhomogeneities in geologic medium (such as fractures) on the scale of the wave lengths of the radar waves are a primary loss mechanism in low conductivity geologic materials. Therefore, it was expected that changes fracture densities would contribute to changes in dissipation of radar energy in the subsurface.

The second physical property to change at intraflow structural boundaries is crystal texture. Long and Wood (1986) found that entablature has feathery, dendritic Fe-Ti oxide crystals, while the colonnade has coarser, cruciform or octahedral Fe-Ti oxide crystals. Degraff et al. (1989) found that entablatures have a greater amount of inclusion-charged glassy mesostasis and smaller average grain size relative to colonnades. Hansen et al., (1973) measured the dielectric properties in two basalt samples of identical composition, with one having a smaller average grain size than the other. The finer grained sample had higher energy loss than the coarser grained sample (Hansen et al., 1973). Thin section data from BLP show a greater abundance of glass in the entablature relative to the other intraflow structures. It was therefore expected that the increased glass content (and inferred smaller crystalline grain size) in the entablature will result in increased attenuation of radar waves.

4.1.3 Determination of Radar Velocity and Attenuation

The travel time of a radar wave in the subsurface is a function of the velocity of the wave in the medium and the distance over which the wave travels. If travel distances are kept constant, the travel times become a function of the radar velocity in the medium. Changes in travel time can then be directly related to changes in the average velocity of the wave through the geologic media. Qualitative analysis of velocity can be made in this way by comparing the arrival times of radar waves recorded at different elevations between a single pair of boreholes. Absolute velocity can be calculated using differences in travel times of radar waves that have traveled different distances. This quantitative

velocity analysis is done by comparing the arrival times of radar waves that have traveled between different pairs of boreholes (with different borehole separations).

Quantitative calculation of radar wave attenuation uses the same method of spectral ratio used to calculate seismic wave attenuation (Equation 3). This method compares the amplitudes of two waves that have traveled different distances through the geologic medium to determine the attenuation of the wave in that medium. As with seismic wave attenuation, use of this equation with radar waves assumes spherical divergence and exponential decay of the waves. In addition, it uses the square root of the spectrum of the autocorrelation of the waveform to remove phase information in the amplitude spectrum. Thus, the attenuation constant, α, in dB/m, of a radar wave is given by:

$$\alpha(f) = -(8.686) \times \frac{1}{R_i - R_j} \times ln\left(\frac{R_i A_i(f)}{R_j A_j(f)}\right) \qquad \text{(EQ 12)}$$

where R_i = distance traveled by wave to receiver position i

R_j = distance traveled by wave to receiver position j

$A_i(f)$ = square root of spectrum of autocorrelation of trace i

$A_j(f)$ = square root of spectrum of autocorrelation of trace j

Turner and Siggins (1994) show that radar attenuation can also be analyzed in terms of a factor, Q*, which is directly analogous to Q used to analyze seismic waves. This new factor Q*, like Q, is a measure of the energy stored to the energy dissipated in a propagating wave. Using a low loss approximation of Equation 10, Turner and Siggins (1994) show that Q* is given by:

$$Q^* = \frac{1}{2v}\frac{\Delta\omega}{\Delta\alpha} \qquad \text{(EQ 13)}$$

where v = phase velocity of the wave.

Thus, Q* is inversely proportional to the slope of an attenuation versus frequency plot.

Turner and Siggins (1994) present laboratory data to show that over narrow frequency ranges applicable to GPR, radar wave attenuation is a linear function of frequency (i.e., Q* is constant). They also show that different geologic media can be distinguished by different values of Q* (Turner and Siggins, 1994). Thus, radar data can be analyzed for changes in the slope of an attenuation versus frequency plot and for changes in Q* as diagnostic of changes in lithology.

4.2 Acquisition

4.2.1 The RAMAC Cross-Borehole Radar System

Cross borehole, ground penetrating radar data were collected using a RAMAC borehole radar system which was developed by ABEM Geosciences, Mala, Sweden (ABEM, 1990). Originally, the system was designed for the detection of fracture sets in crystalline rock, as part of the Stripa project (ABEM, 1990). (Stripa was a large scale project to research placing nuclear waste repositories in granitic rock near the town of Stripa, Sweden). The RAMAC borehole radar is designed to operate in boreholes up to 1000 m deep. Proprietary software written by the manufacture allows for automated collection, processing, and interpretation of radar data.

Figure 4.1 is a schematic diagram of the data collection system. The receiver and transmitter are housed with their respective antenna in borehole sondes; a detachable

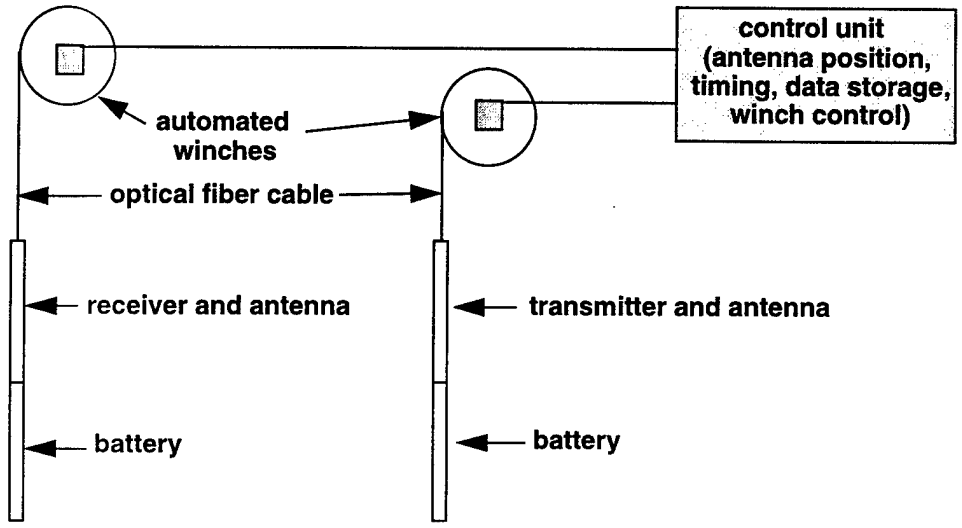

Figure 4.1 Equipment diagram for borehole radar data collection. The receiver and transmitter are each housed with their respective antenna in a borehole sonde, attached to which is a battery. The tools are connected to the control unit by fiber optic cable which is wound with the supporting kevlar cord around an automated winch. The control unit calculates antenna positions and then controls the winch to put them in position for measurements. The control unit also determines transmitter firing and receiver sampling times and stores data collected by the receiver.

battery is attached below each antenna unit. Each antenna-battery package is ~4 meters in length. The transmitter and antenna are connected to the control unit through 1000 m of optical fiber. The fiber and supporting kevlar cord are wound on an automated winch. The control unit, loaded with the manufacture's software, sets timing for the transmitter and receiver, stores data sent from the receiver, and controls the winches.

4.2.2 Data Acquisition

Two basic experiment configurations were used in data collection: *level runs* and *tomographic surveys*. Figure 4.2 shows how antenna are positioned in these configurations. For level runs, the transmitter and receiver antenna were kept at the same elevation in separate boreholes. After a measurement is taken, both tools move to the next elevation. The distance an antenna moves between measurements is called the *step*. For tomographic surveys, one antenna is held fixed while the other moves through a series of positions, at each of which a measurement is taken. This series of positions is called a *fan*. The fixed antenna is then moved to another position, and the moving antenna sweeps out another fan. The group of measurements taken in one fan are called a *tomographic scan* (or just *scan*).

Data were collected between five combinations of the four boreholes, with nominal separations of 15, 20, 25, 30, and 35 m. Data were generally not collected above ~932 m elevation due to poor signal reception. Because of the length of the antenna-battery combination, data could not be collected at the bottom of each hole. Therefore, data were not collected below 911 m elevation.

4.3 Processing

4.3.1 Data Sorting

For purposes of processing and discussion, experiments and data sets were named to describe the antenna configurations and boreholes used in the experiment. An "L" or "T" is used to designate a level run or tomographic data set, these are followed by the numbers

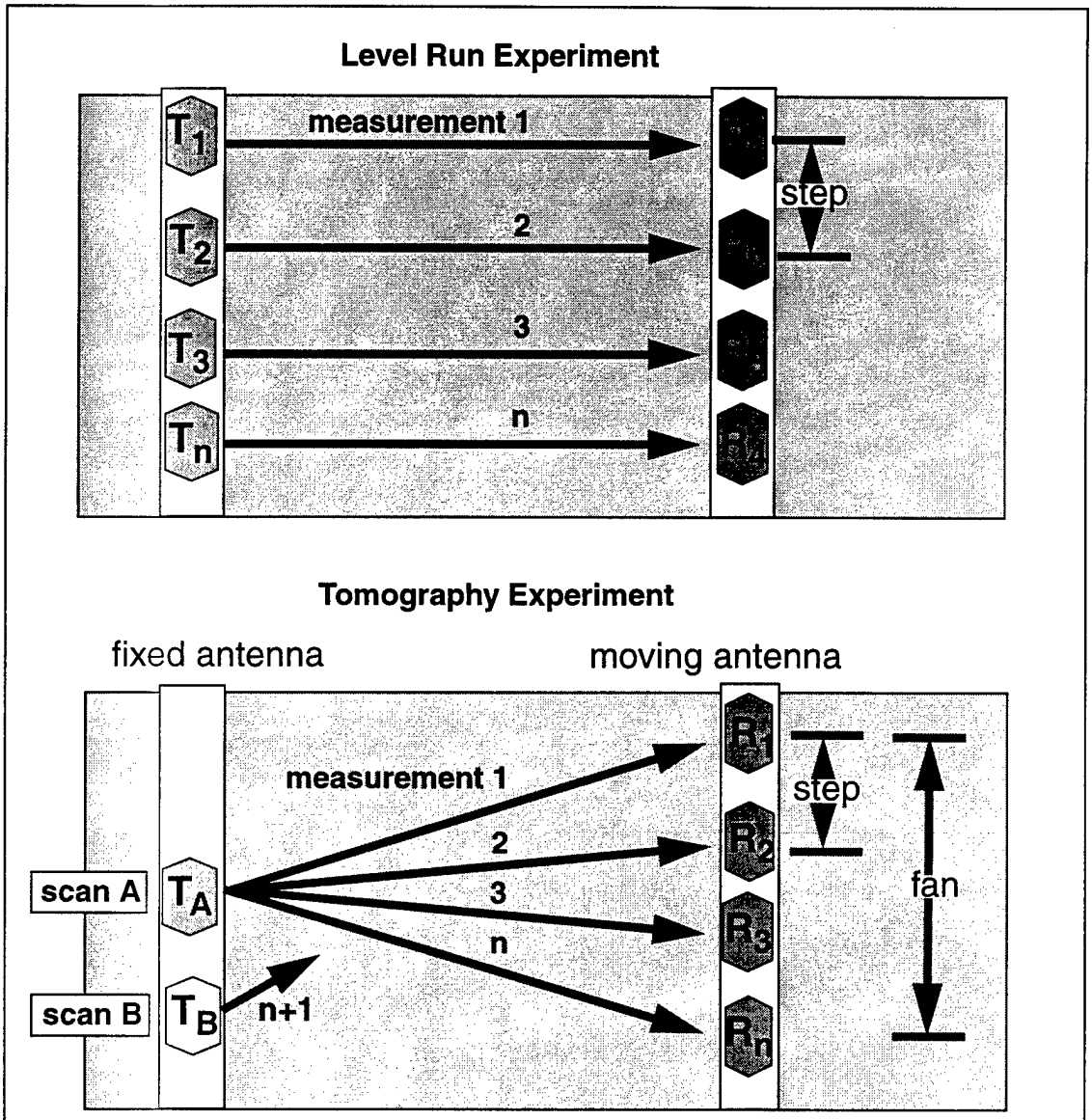

Figure 4.2 Borehole radar data collection diagrams: level run experiment (top), tomography experiment (bottom). In level run experiments, the transmitter (T) and receiver (R) antenna are kept level as measurements are taken down the borehole. In tomography experiments, one antenna is kept at a fixed position, while the other moves between measurements. A "scan" is the set of measurements collected from a single position of the fixed antenna. The "fan" is the +/- distance of the moving antennas position's relative to the fixed antenna in one scan. Step size is the distance the antennas move between measurements.

of the boreholes used in the experiment. Thus, L12 is a level run experiment between BH1 and BH2; T13 is a tomographic survey between BH1 and BH3. L21 was conducted between BH1 and BH2, with the transmitting and receiver antenna in reversed holes from L12. Two additional data sets were created during processing: TL12 and TL13. These files were made by selecting the traces in T12 and T13 in which the antenna positions were level.

4.3.2 Removal of Receiver Drift

Inspection of raw traces showed a consistent, low frequency drift imprinted over the signal in each trace. Plotted in Figure 4.3 is a typical, unfiltered trace ("observed data"). The drop in amplitude near the end of the trace is the drift that contaminated all traces, most significantly traces with relatively weak signal. Removal of this drift is accomplished by fitting a fifth order polynomial to the trace, then subtracting it from the trace. Superimposed on the unfiltered trace in Figure 4.3 is the polynomial fitted to that trace. The upper, "drift corrected" trace in the figure is the same trace with the polynomial subtracted from it. One effect of this processing step is to remove all information below ~1 MHz in the amplitude frequency spectra. Drift removal was the first step in most subsequent data processing and plotting.

Plots of the level run data are shown in Figure 4.4. In the figure, drift was removed as described above, a butterworth filter was applied, and then each trace was individually gained. The pass band of the butterworth filter was 15 - 80 MHz for L12, L13, and L14. The pass band was 15 - 60 Mhz for L23. Elevations are in meters above sea level. Zero time in these plots is not the time of transmitter firing, it represents the first sample taken

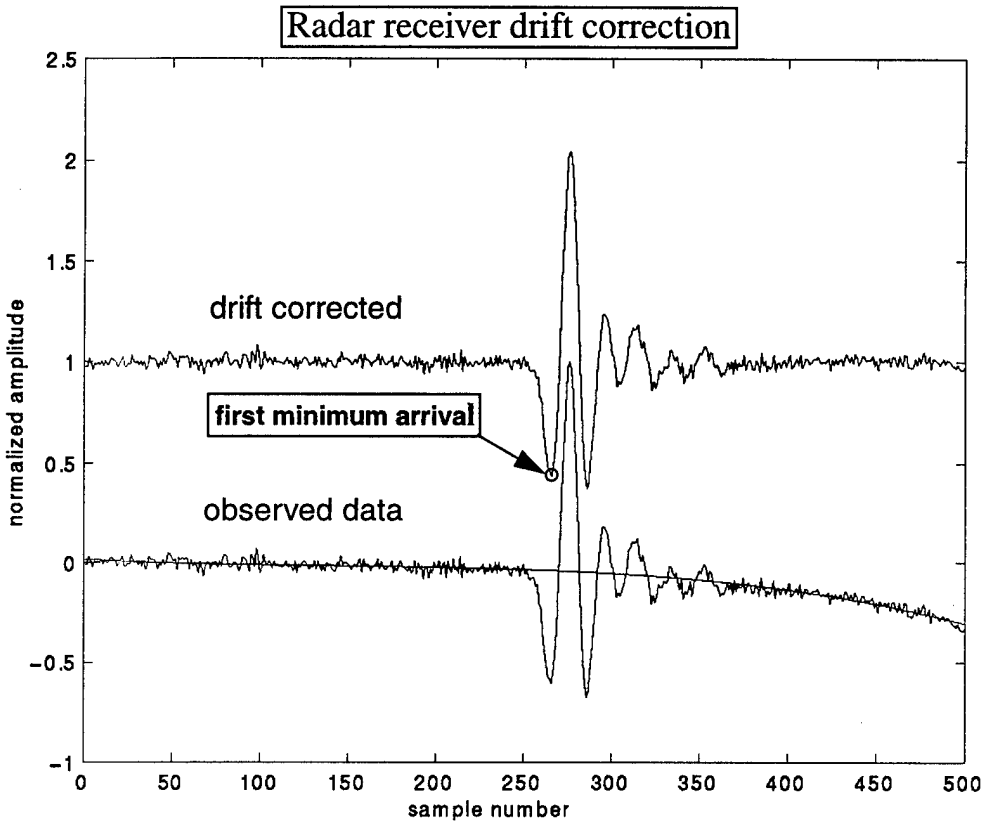

Figure 4.3 Example of drift correction. The "observed data" is an unfiltered trace from L13 with a fifth order least squares fit line superimposed. The drop in amplitude near the end of each trace leaves a low frequency artifact in the frequency spectrum of the trace. This artifact is effectively removed by subtracting the superimposed polynomial from the trace. The "drift corrected" trace is the result of the subtraction process. All subsequent plots of level run data have been processed in this manner unless otherwise noted. Also shown in the location of the first minimum arrival, which is used for velocity analysis.

by the receiver (this will be discussed more thoroughly in section 4.3.3). Relative time, in seconds, is calculated by dividing the number of samples in each trace by the sampling frequency used in the experiment.

Plots of data from tomographic surveys T12 and T13 are shown in Figure 4.5. In these plots, shading represents the amplitude of the received signal. Each tomographic

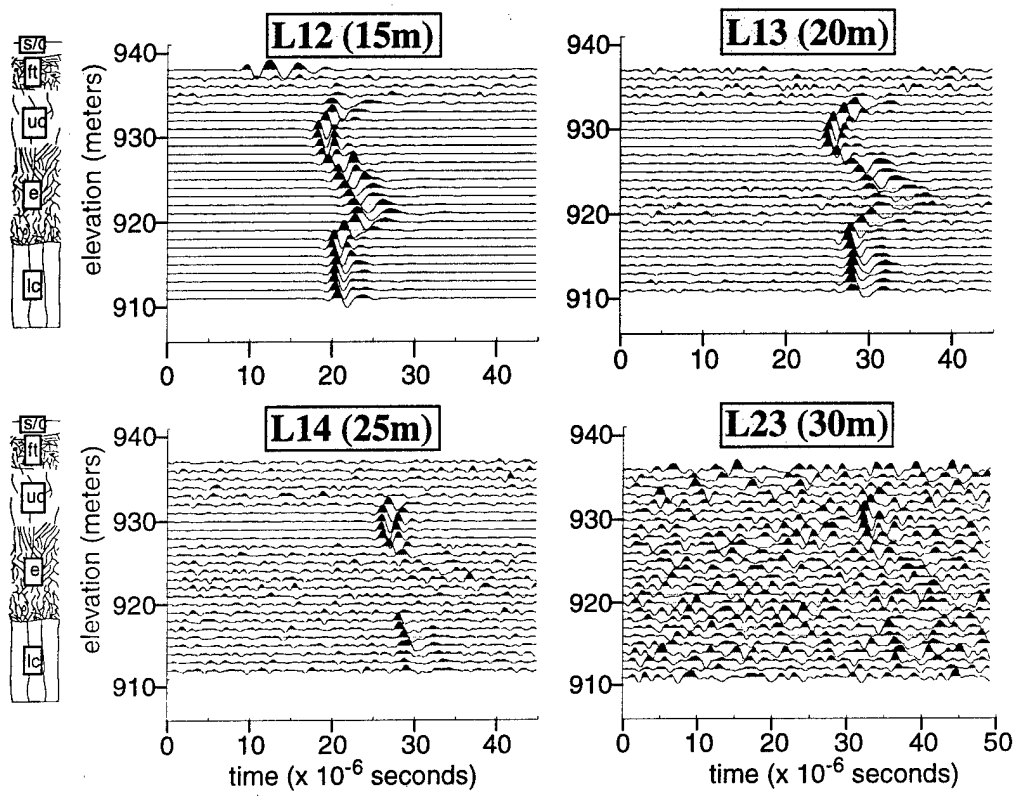

Figure 4.4 Level run experiments data plots. Plotted are the data records from four level run experiments (the nominal borehole separation is shown in parenthesis). Each trace has been drift corrected and individually gained. A consistent pattern of arrival times versus elevation is seen in the records. The relative arrival times in an individual record is indicative of changing velocity in the subsurface. In each record, the signal-to-noise ratio is greatest between 927-934 m elevation (upper colonnade), and smallest between 919-925 m elevation (entablature). The relative signal to noise ratio in each record is indicative changing attenuation in the subsurface.

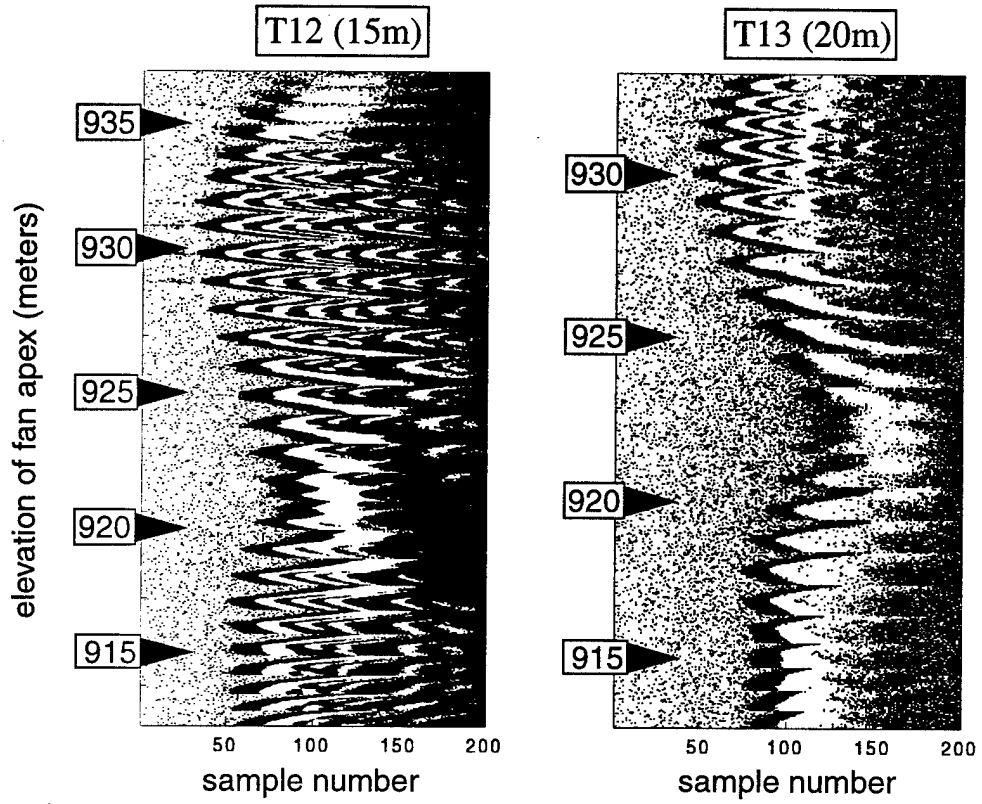

Figure 4.5 Tomography data T12 and T13. Plotted are traces from tomographic data collection, nominal borehole separations are shown in parenthesis. In the plot, individual traces are plotted horizontally. A group of traces from one tomographic scan forms a hyperbola in the plots. Shading represents amplitude of signal. The apex of each hyperbola is located where the transmitting and receiving antenna are at the same elevation. Selected apex elevations are shown with boxes and arrows. Because of differing parameters during data collection, the two depth scales do not line up. The times of the apex arrivals follow a similar pattern to the arrivals seen in the level run plots (Figure 4.4), which is indicative of velocity change with elevation in the subsurface.

scan is seen as a hyperbola in the plot, the apex of which is at the elevation of the fixed antenna. Shown in the boxes with arrows are selected fixed antenna elevations. Traces above the apex within each scan represent higher elevations of the moving antenna relative to the fixed antenna, traces below the apex represent lower elevations of the moving antenna.

4.3.3 Calculation of Radar Velocities

Inspection of the individual data records in Figure 4.4 indicates a consistent change in velocity with elevation in the subsurface. This qualitative analysis is based on the consistently later arrival of the signal in the entablature relative to the upper- or lower colonnade. While this velocity change is fairly easy to see in the data records, quantifying it requires considerable effort, as described below.

The RAMAC borehole radar system, like most GPR systems, creates each trace by firing the transmitter multiple times, recording only one sample per firing. Thus, each trace in the data presented here represents a composite of 512 firings of the transmitter and 512 samplings of the receiver. This method of data recording, known as equivalent time sampling, does not allow for precise measurement of the "time" between transmitter firing and the beginning of the recording window. For this reason, time zero in the radar records (Figure 4.4) is not the time of transmitter firing during data collection, it is only the start time of receiver sampling.

Although the absolute time of transmitter firing relative to the recording window can not be determined from the collected data, relationships in the data can be exploited to

determine velocity. Figure 4.6 shows the timing relationship used by the data collection software. *Signal position* is time the transmitter is fired relative to the internal clock of the control unit. Signal position is adjusted at the start of data collection so that the radar pulse arrives at the receiver in the recording window. The break in the time line between signal position and the recording window in Figure 4.6 represents the sum of the unknown travel time of the trigger pulse from the control unit to the transmitter, plus that portion, if any, of the actual travel time of the radar pulse in the subsurface before the receiver began sampling. This unknown time correction is denoted by Δt_n.

For two traces corresponding to waves that traveled different distances through the same medium, the velocity of the waves is given by:

$$v = \frac{(d_1 - d_2)}{(\Delta t_1 + t_1) - (\Delta t_2 + t_2)} \qquad \text{(EQ 14)}$$

where d_1 = distance traveled by wave 1

d_2 = distance traveled by wave 2

t_1=arrival time of wave traveling distance d_1.

t_2=arrival time of wave traveling distance d_2.

Δt_1=unknown time correction for wave 1

Δt_2=unknown time correction for wave 2.

Because L12 and L13 were collected with the same signal position, Δt_1 equals Δt_2 (this assumption is considered further in section 4.3.4). Assuming azimuthal isotropy, any difference in arrival times of the signals at any one elevation in these records is thus a function of the difference in travel distances and travel times given by:

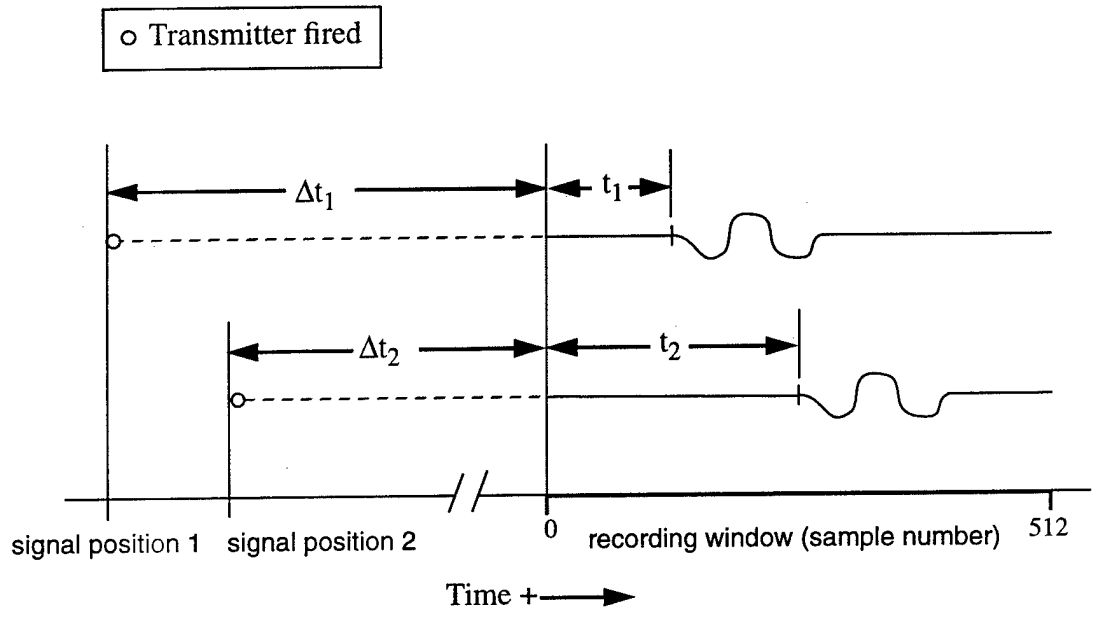

Figure 4.6 Timing diagram for data collection. Shown are the relative temporal positions of the transmitter firing, the recording window, and the signal arrival. Signal position is the time the transmitter is fired relative to the internal clock of the control unit; Δt is the unknown time interval between the firing of the trigger pulse and the start of the recording window; t is the arrival time relative to the recording window.

$$v = \frac{(d_1 - d_2)}{(t_1 - t_2)} \qquad \text{(EQ 15)}$$

where d_1 = travel distance for L12 (14.59 m)

d_2 = travel distance for L13 (20.25 m)

t_1 = arrival time of signal in recording window for L12

t_2 = arrival time of signal in recording window for L13.

Equation 14 uses differences in arrival times. As long as these times were measured from the same time datum (i.e. $\Delta t_1=\Delta t_2$), the individual value of t_1 and t_2 are not relevant, only the difference between them. For this reason, the arrival time of the signal minima can be used in the analysis rather than the first break. Because of background noise, the arrival time of the signal minimum is more accurately picked than the time of the first break (Figure 4.3). The signal minimum is early in the waveform where any dispersion effects are considered negligible. Use of the minimum in this analysis also assumes negligible difference in waveform between L12 and L13.

Figure 4.7 is a plot of the calculated velocity versus depth in the subsurface. Velocity was calculated using the difference in arrival time of the signal minima and the difference in travel distance between L12 and L13. In the plot it is seen that velocity is greatest at approximately 928 meters elevation ($V=\sim 9 \times 10^7$ m/s), and lowest at approximately 922 meters depth ($V=\sim 6.5 \times 10^7$ m/s). Velocity is fairly constant below 920 m elevation, above this it changes continually.

4.3.4 Velocity Error Analysis

Error bars on the velocity values in Figure 4.7 account for inherent inaccuracies in the measurements that go into calculating velocity. Inspection of Equation 14 shows six variables are used to calculate velocity: d_1, d_2, t_1, t_2, Δt_1, and Δt_2. The first four of these are physically measured. The last two are assumed equal, and cancel out of the equation. However, deviation from this assumption is known to occur in GPR data ("firing time chatter"), therefore, error in the assumption of equality will be accounted for in the error

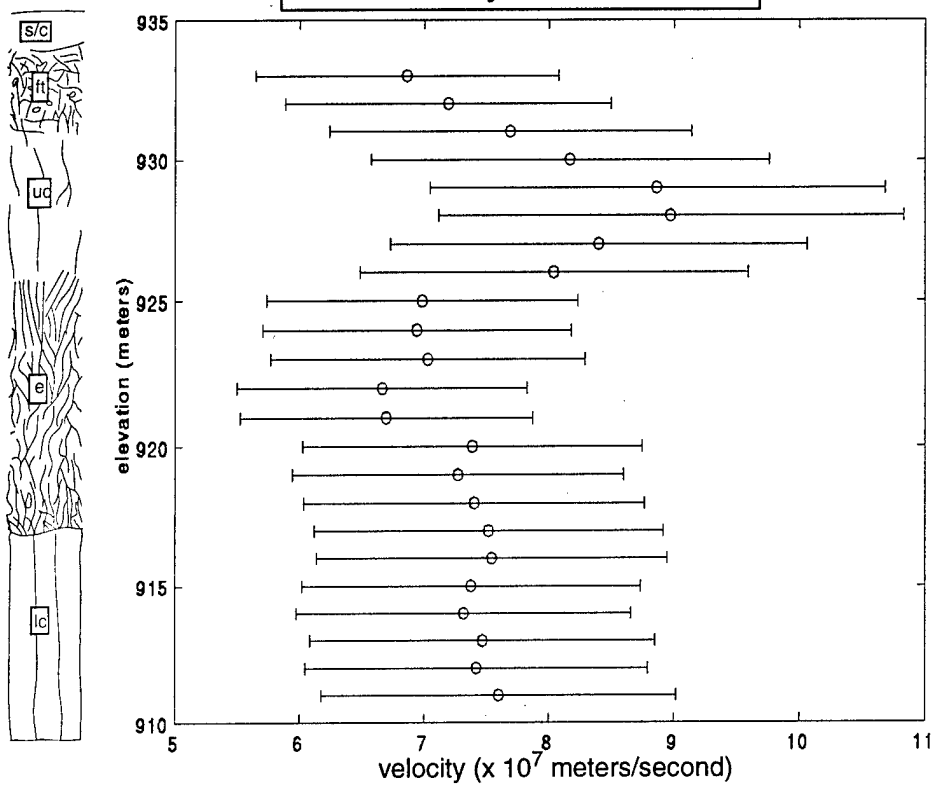

Figure 4.7 Radar velocity versus elevation. Velocity was calculated at each depth from the difference in arrival time at that depth and the difference in travel distance between L12 and L13. Error bars in this plot represent 95% confidence intervals and take into account errors in picking arrivals (+/- 0.03 x 10^{-7} seconds), errors in travel distance (+/- 0.5 meters), and errors in signal position (0.03 x 10^{-7} seconds). Inspection of the figure shows the velocity maximum is at 928 meters elevation, and the velocity minimum is at 922 meters elevation, although the error bars do not allow this difference in velocity to be called statistically significant.

analysis of the velocity. Since no actual measurements are made of Δt_1 and Δt_2, they can be combined into a single term for error analysis:

$$\Delta T = \Delta t_1 - \Delta t_2 \qquad \text{(EQ 16)}$$

Substituting this into Equation 14 results in

$$v = \frac{(d_1 - d_2)}{\Delta T + (t_1 - t_2)} \qquad \text{(EQ 17)}$$

Assuming uncorrelated errors in measuring the variables, the estimate of the variance of velocity, σ_v, is given by:

$$\sigma_v = (A + B)^{\frac{1}{2}} \qquad \text{(EQ 18)}$$

where

$$A = \left(\frac{\partial v}{\partial d_1}\right)^2 (\sigma_{d_1})^2 + \left(\frac{\partial v}{\partial d_2}\right)^2 (\sigma_{d_2})^2 \qquad \text{(EQ 19)}$$

and

$$B = \left(\frac{\partial v}{\partial \Delta T}\right)^2 (\sigma_{\Delta T})^2 + \left(\frac{\partial v}{\partial t_1}\right)^2 (\sigma_{t_1})^2 + \left(\frac{\partial v}{\partial t_2}\right)^2 (\sigma_{t_2})^2 \qquad \text{(EQ 20)}$$

and

σ_{d1} = +/- error in d_1

σ_{d2} = +/- error in d_2

$\sigma_{\Delta T}$ = +/- error in ΔT

σ_{t1} = +/- error in t_1

σ_{t2} = +/- error in t_2

The +/- error in the d_1 and d_2 must take into account the inaccuracy in measuring the location of the boreholes on the surface, and the deviation from vertical of the boreholes. Locations on the surface were measured with the Topcon survey instrument. This tool is capable of measuring positions to the nearest 0.001 mm; although field procedures used did not achieve this accuracy. The locations of the all the boreholes were surveyed on two separate occasions; the positions of each borehole agree to within 0.05 m in these surveys. Calculations of the separation between BH1 and BH2 using each survey agree to within 0.11 m; between BH1 and BH3, they agree to within 0.08 m. No measurements were made of borehole deviation. An assumed error in the travel distances of +/- 0.5 m is used in the errorbar calculations, which is considered highly conservative.

The +/- error in picking arrival times must take into account errors in identifying the same point on the waveform between traces, errors in picking the exact sample in which the waveform arrived, and the finite time width of that sample. As explained earlier, the arrival of the minimum of each trace was used in calculation. Figure 4.3 shows that this arrival is relatively easy to identify over background noise, and the sample of its arrival is easier to pick than for the first break. Using this arrival assumed little change in the waveform from trace to trace. Close examination of the waveform showed that a +/- three sample error was reasonable for picking the arrival. For the data in Figure 4.3, the sample rate was ~0.001 μs, giving an estimated +/- error for the arrival time of 0.003 μs, which is considered conservative.

Determining the +/- error of ΔT (or, Δt_1 and Δt_2) was more intractable than the errors in the direct measurements. ΔT is the difference in timing of transmitter firing between

two traces, as recorded in the signal position times. Signal position is determined by the relationship between periodic voltage curves generated by the control unit. A check of possible drift in this timing relationship can be made by using the calculated velocities to "back calculate" Δt_n. Inspection of Figure 4.6 shows that the actual travel time of the wave in the subsurface, which will be denoted by T, is given by:

$$T = \Delta t + t \qquad \text{(EQ 21)}$$

Assuming straight ray paths, the actual travel time, T, is also equal to the ratio of the true travel distance, d, and the true velocity, v:

$$T = \frac{d}{v} \qquad \text{(EQ 22)}$$

Rearranging Equation 21 and substituting the relationship into Equation 22, Δt is given by:

$$\Delta t = \frac{d}{v} - t \qquad \text{(EQ 23)}$$

Figure 4.8 is a plot of Δt for L21, calculated using Equation 23. Since the true distances and velocities are not known, the measured distance and calculated velocity between L12 and L13 were used. Inspection of Figure 4.8 shows Δt does vary from trace to trace. One standard deviation for Δt in this plot is ~0.01 μs. The +/- error calculated for the velocity with Equation 18 (3.5×10^6 m/s) used an estimated $\sigma_{\Delta T}$ of 0.03×10^{-7}. Using the previously given +/- errors for the distance and arrival time, and taking the +/- error calculated for the velocity from Equation 18, the expected variation in Δt is ~0.01 μs. That the predicted variation of Δt, which used an estimated signal position error, agrees

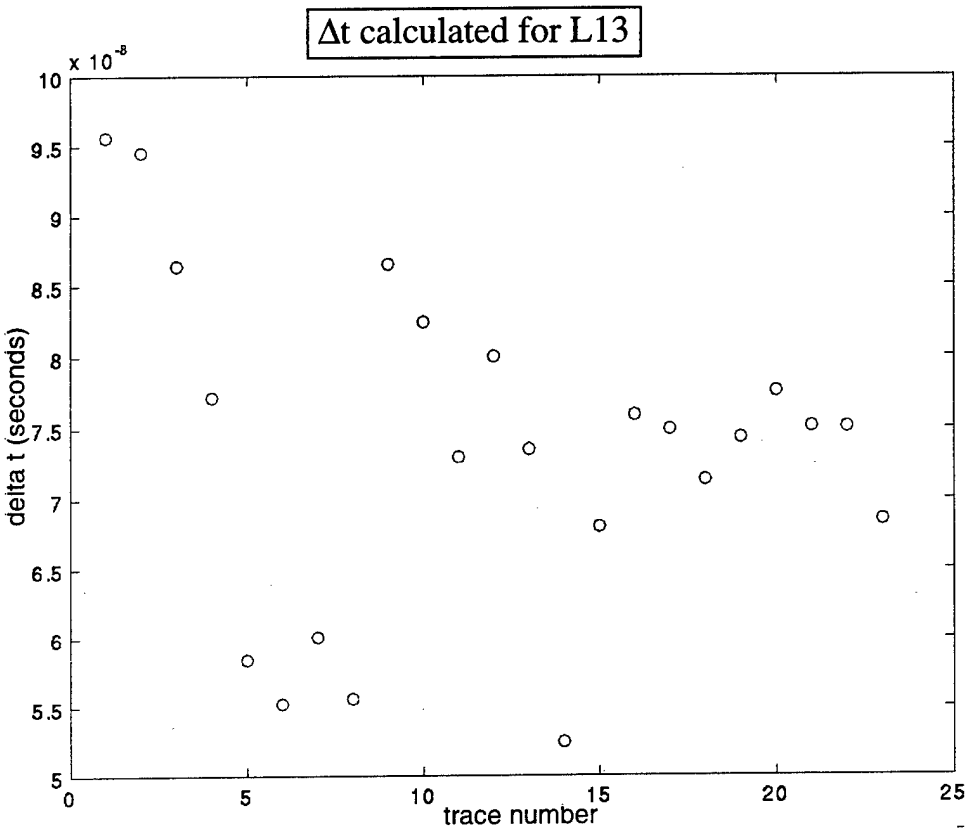

Figure 4.8 Calculated Δt for L13. Δt was back calculated from the velocities at each elevation obtained from comparison of arrival times in L12 and L13. Δt should be constant for all depth. The standard deviation for Δt in this plot is ~0.01 μs. Using estimated errors in distances, velocities, and arrival times used to calculate Δt, the expected deviation in these values is ~0.01 μs.

well with the calculated variation, suggests that all errors are being adequately accounted for.

The error bars on the velocity in Figure 4.7 were calculated using conservative estimates of errors in measured parameters. It is likely that the actual error in the parameters is less than estimated, and that more and better measurements would decrease

the size of the error bars. Based on visual inspection of the data records, it is concluded that the change in velocity between the intraflow structures may be real, although the error bars do not allow it to be called significant.

4.3.5 Determination of Radar Wave Attenuation

Loss of energy in a propagating radar wave can be caused by attenuation inherent in the geologic media and/or by scatter of the energy from fractures and other inhomogeneities. As discussed above, loss from both of these mechanisms was expected to be greater in the entablature than in either the upper- or lower-colonnade.

Figure 4.9 shows the normalized power spectra of the data in L12, L13, and L14 (center frequency of the radar antenna used to collect the data was 60 MHz). Inspection of Figure 4.9 shows a loss of high frequencies in the entablature between approximately 919 and 927 meters elevation in each record, which corresponds to a drop in the signal to noise ratio in the entablature in each level run data record shown in Figure 4.4. This qualitative analysis of attenuation indicates a greater loss of radar signal in the entablature compared to the upper- or lower-colonnade

Quantitative calculation of attenuation was done using the method of spectral ratios described in section 4.1.3. Figure 4.10 is a comparison of the calculated attenuation constants of the received radar signal in the upper colonnade, entablature, and lower colonnade. The elevations of the center of each structure were assumed equal to outcrop (Figure 2.5). Also plotted are averaged, normalized spectra of three traces centered on

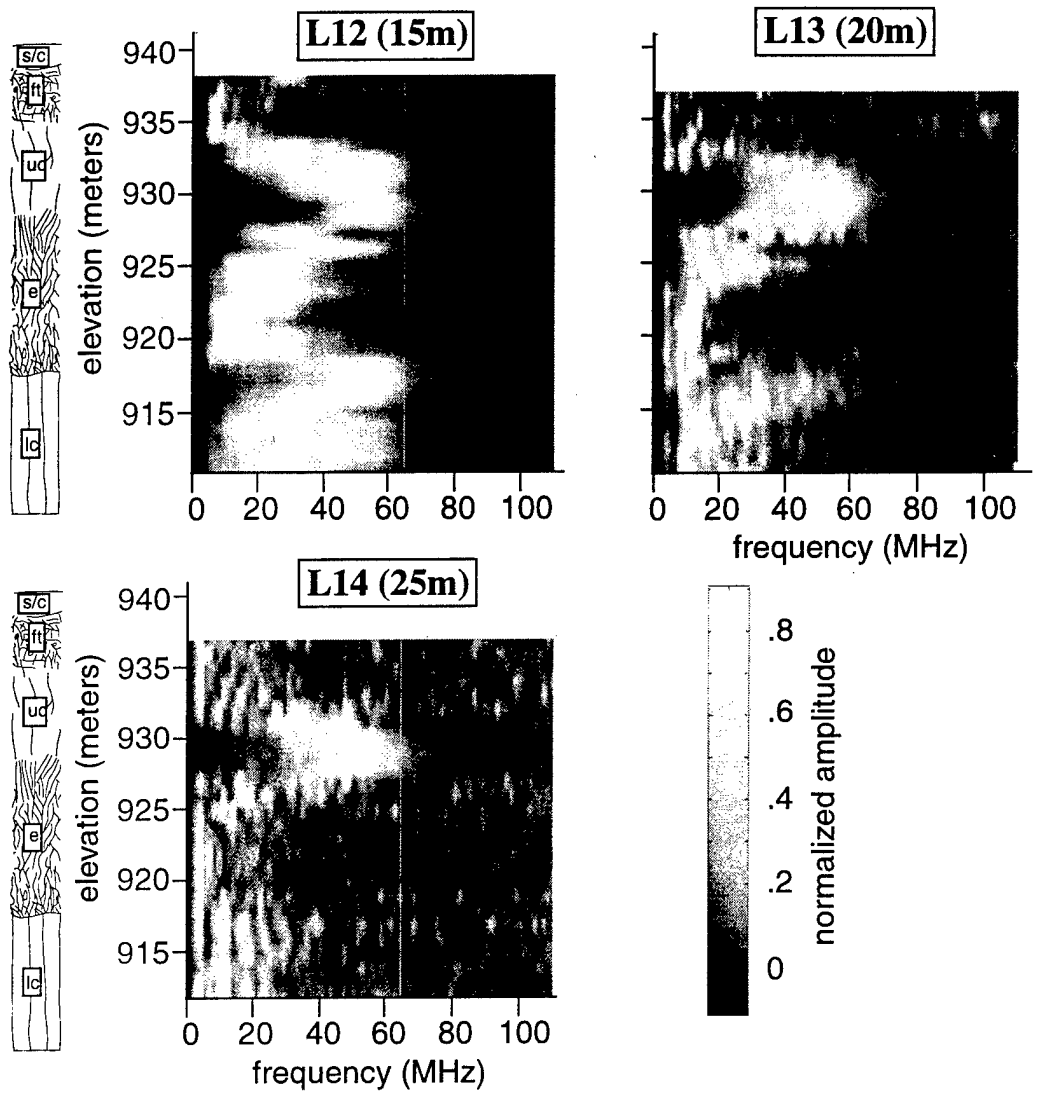

Figure 4.9 Power spectra of L12, L13, L14 (nominal borehole separations are shown in parenthesis). For these plots, receiver drift was removed before spectra were calculated. Each spectra trace was individually normalized in these plots. Center frequency of the radar antenna was 60 MHz. In each data set, strong signal between ~40 and 60 MHz is seen between approximately 927 and 933 m elevation. More noise is visible in the normalized traces of L14, than L13, which itself has more noise than L12.

these elevations from L12 and L13. A first order polynomial was fit to the attenuation constant between approximately 7 and 70 MHz, the slope of this polynomial is listed.

Equation 13 gives a formula for calculating Q* for each intraflow structure. Using the slope from Figure 4.10, and the velocity from Figure 4.7, a Q* value was calculated for each intraflow structure. For the upper and lower colonnade, Q* is equal to 0.19 and 0.39, respectively. For the entablature, Q* is equal to 8.3. Similar numbers in the upper and lower colonnade suggest similar attenuation in these intraflow structures, and a different attenuation in the entablature.

Error bars on α in Figure 4.10 were derived from the measurements of the variations in amplitude of received signals which traveled over the same ray path. Between BH1 and BH2, four separate recordings were made at 10 m depth. Between BH1 and BH3, three separate recordings were made at 10 m depth. A Student's t distribution was assumed for the deviation of the variation in amplitude of the received signal between each pair of boreholes. The deviation was made the +/- error in the amplitude measurement, σ_A. The +/- error in the attenuation constant, σ_α, is then by:

$$\sigma_\alpha = \sqrt{\left(\frac{\partial \alpha}{\partial A_i}\right)^2 (\sigma_{A_i})^2 + \left(\frac{\partial \alpha}{\partial A_j}\right)^2 (\sigma_{A_j})^2} \qquad \text{(EQ 24)}$$

where σ_{Ai} = standard deviation of amplitude in L13

σ_{Aj} = standard deviation of amplitude in L13

and

$$\frac{\partial \alpha}{\partial A_i} = \frac{20}{2.3} \times \left(\frac{1}{r_1 - r_2}\right) \times \left(\frac{-1}{A_j}\right) \qquad \text{(EQ 25)}$$

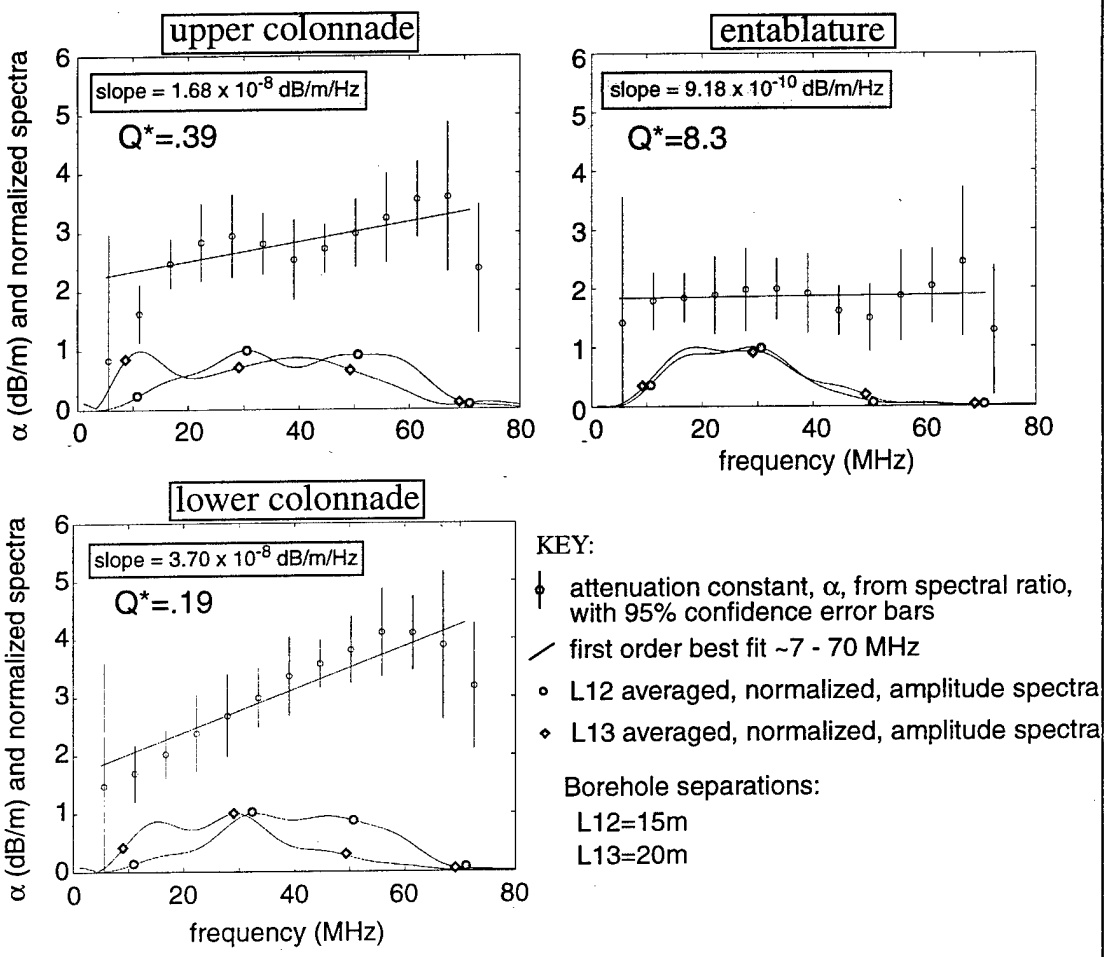

Figure 4.10 Attenuation constant and averaged power spectra for intraflow structures. Shown are the normalized amplitude spectra calculated by averaging the spectra of three traces at the center of each intraflow structure. The attenuation coefficient, α, was calculated using the ratio of un-normalized amplitude spectra and the difference in travel distance between L12 and L13. Error bars on α were derived from a Student's t distribution of the variation in measurements of the amplitude of received signal over the same ray path. A first order polynomial was fit to α between ~7 and 70 MHz, the slope of this line was used to calculate Q* by Equation 12. As discussed in the Section 4.4.1, the value of slope and corresponding Q* value of the entablature are considered misleading due to calculations based on low signal strength in the received signal.

$$\frac{\partial \alpha}{\partial A_j} = \frac{20}{2.3} \times \left(\frac{1}{r_1 - r_2}\right) \times \left(\frac{-1}{A_i}\right) \qquad \text{(EQ 26)}$$

It is important to note that σ_α was calculated as a function of frequency at one depth only. Error in α at other depths is assumed equal to that at 10 m depth.

In order to compare radar attenuation at all elevations, the mean attenuation coefficient between 10 and 70 MHz was calculated for each elevation. Figure 4.11 is a plot of the mean α value over this frequency range for each elevation. For the plot, the mean α value at each elevation was averaged with the adjacent elevations to smooth variations in the plot. Error bars represent two standard deviations in the variation of α over the frequency range at that elevation. Inspection of Figure 4.11 shows the calculated mean attenuation coefficient appears lower in the entablature compared to the lower colonnade and most of the upper colonnade, however this result is considered misleading and will be discussed further below. The trend towards lower attenuation at the top of the upper colonnade is likely the result of α being calculated over a window that includes the flow top, through which little or no signal was received. Similar to problems with calculating Q*, comparing signals that are very nearly zero can result in an apparent increase in signal strength with distance (i.e. a negative α value).

4.4 Interpretation

4.4.1 Correlation of Radar Results with Geology

Error bars in Figure 4.7 are large, partly due to the conservative estimates of unknown parameters used to calculate them. Despite this, velocity can be seen to change between the intraflow structures. Using the geologic column for reference (Figure 4.7), velocity is

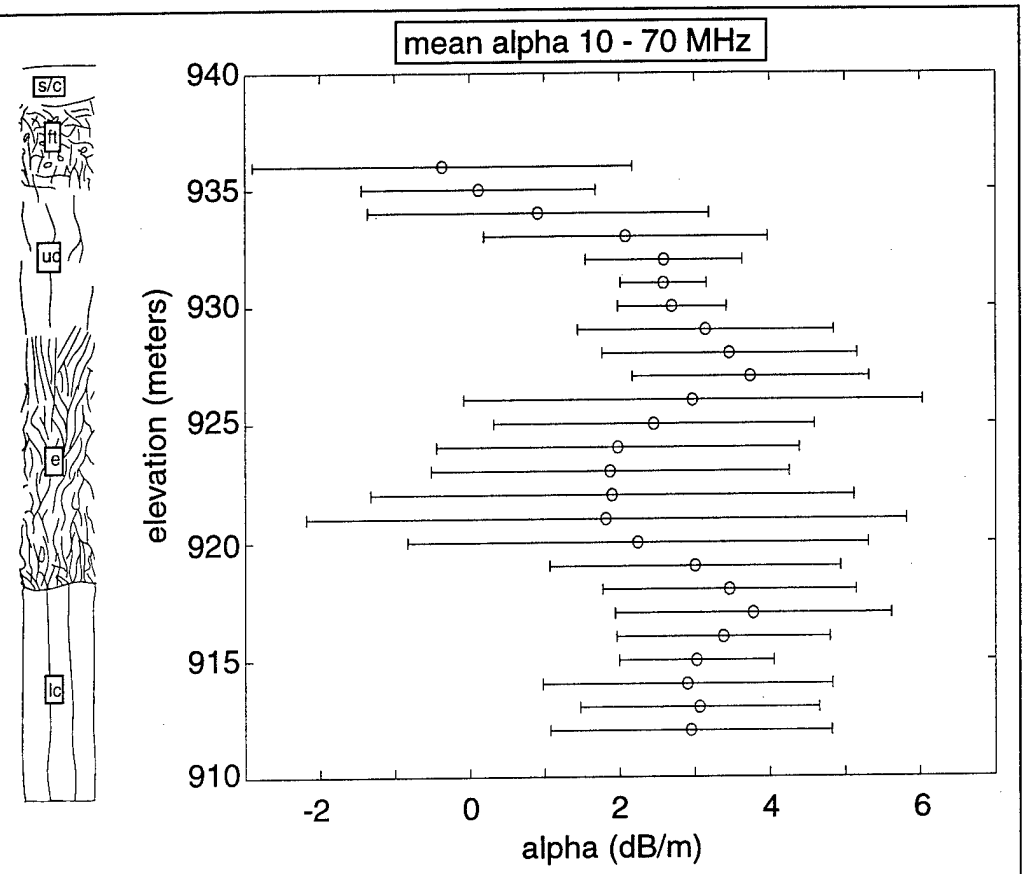

Figure 4.11 Mean radar attenuation between 10 and 70 MHz. Mean alpha values between 10 and 70 MHz at each elevation were determined, and then averaged with the two adjacent elevations. Error bars represent two standard deviations of the variation of alpha between 10 and 70 MHz at the elevation plotted. Mean alpha values show generally lower attenuation in the entablature compared to the lower colonnade, however this is considered misleading because of the limits of the method used to calculate attenuation. The trend to lower alpha values at the top of the upper colonnade is attributed to effect of little to no signal reception in the flow top.

greatest in the upper colonnade and slowest in the entablature. Although these velocity variations occur within overlapping error bars, the very similar relative arrival patterns in the records in Figure 4.4 and Figure 4.5 suggests that the changes in velocity are real. This conclusion is strengthened by noting that the velocities changes in Figure 4.7 correlate with differences in the arrival times in the data records (Figure 4.4). Azimuthal isotropy

was assumed for calculating velocity; the consistent pattern of arrivals in the records in Figure 4.4, which were collected at widely different azimuths, validate this assumption.

The calculated velocities within the basalt vary between ~6.5 x 10^7 m/s and 9 x 10^7 m/s, which are very near or equal to the predicted velocity based on hand sample measurements of dielectric permittivity, bulk measurement of conductivity, and estimate of magnetic permeability (section 4.1.2). That velocity does change between the intraflow units suggests that one or more of these parameters change in the bulk formation between these intraflow structures. The changes in the "bulk parameters" may be a function of changes inherent in the basalt, such as crystal grain size, or they may be a function of changes in fracture characteristics, such as number, aperture, and/or infilling materials. The analysis presented here does not allow for clear separation of these effects on the measured radar velocities.

Figure 4.10 shows that attenuation also changes between the different intraflow structures. Using Q* to describe attenuation, Figure 4.10 shows that the upper and lower colonnade have a similar attenuation when compared to the entablature. This similarity is confirmed in the similar spectra from these intraflow structures in Figure 4.9. However, the relatively large Q* value of the entablature suggests less attenuation in this intraflow structure compared to the upper or lower colonnade. This is result is considered misleading and is attributed to calculations based on very low received signal strength (as discussed below).

Figure 4.11 shows comparisons of the calculated attenuation at each elevation. Ignoring the very top of the upper colonnade, for reasons discussed above, the lowest

attenuation in the basalt flow appears to be in the entablature. This result is consistent with the calculations of Q* shown in Figure 4.10, however, as with the Q* value for the entablature, it is considered misleading. The relatively large error bars in Figure 4.11 do not allow for the changes in the calculated mean alpha to be called statistically significant. However, the distinct change in the mean value at the upper and lower boundaries of the entablature is considered indicative of "different" attenuation in this intraflow structure.

Qualitative evidence of the difference in radar energy loss between intraflow structures is evident in the level run records (Figure 4.4) and the amplitude spectra (Figure 4.9). Although calculations of Q* and α suggest less attenuation in the entablature, inspection of Figure 4.4 shows that the signal to noise ratio is lowest in all the records in the entablature, suggesting the greatest attenuation is in this intraflow structure. In addition, inspection of Figure 4.9 shows virtually no received energy above ~50 Hz in the entablature in any of the records. For the greater transmitter to receiver separations in L13 and L14, the energy cut-off occurs at progressively lower frequencies. This loss affects the calculation of Q* and mean α, because both are based on ratios of amplitudes out to ~70 MHz. When the signals being compared lose all energy above a certain frequency, this amplitude ratio becomes essentially one, resulting in "low" attenuation values. Additionally, when signal strength is near zero, the ratio becomes one of noise amplitudes and does not give information on the rock matrix.

The calculated attenuation values do not agree well with the predicted estimate of attenuation based on hand sample measurements of dielectric permittivity, bulk measurement of conductivity, and estimate of magnetic permeability. As discussed above,

it is likely that the actual attenuation of radar in basalt is more complex than the calculated values are indicating. Also, confounding factors such as fracture infilling materials and groundwater infiltration further complicate the interpretation.

The results presented here show that velocity and attenuation of radar energy are different in each intraflow structure. Conservative estimates on the precision of the factors used to calculate velocity result in large error bars, limiting what can be said of the statistical significance of the velocity values. Calculations of radar attenuation gave apparently misleading results, i.e. high Q* and low mean α values indicating low attenuation in entablature, and yet low signal to noise ratios and large loss of higher frequencies in the entablature indicating high attenuation in this structure. Despite the contradictory attenuation information in the entablature, the upper and lower colonnade show similar patterns of velocity and attenuation which are different from the velocity and attenuation seen in the entablature. Accounting for the physical mechanisms responsible for the results presented here is a prime topic for future research.

5. DISCUSSION AND CONCLUSIONS

5.1 Summary of Results

Results of the various methods used on the basalt of Lucky Peak to distinguish intraflow structure are shown in Figure 5.1. For reference, a geologic column is included, and the elevations of the intraflow structural boundaries are indicated with horizontal dashed lines. Plotted in Figure 5.1 are the fracture density from BH1 core, the modal composition of glass in thin sections, the mean relative dielectric permittivity measured in hand samples, the electrical resistivity of the subsurface from TDEM data, the seismic P- and S-wave velocity, the seismic P-wave attenuation coefficient, the radar wave velocity, and the mean radar α value. Error bars were not included in this figure for purposes of clarity.

Significant results of this study include:

- fracture density measured in core does not correspond to what is expected based on visual inspection of outcrop;
- entablature has a higher modal composition of glass than the lower colonnade;
- surface electrical resistivity methods do not show resistivity changes within the flow;
- P- and S-wave seismic velocities are greater in the entablature and lower colonnade compared to the upper colonnade;

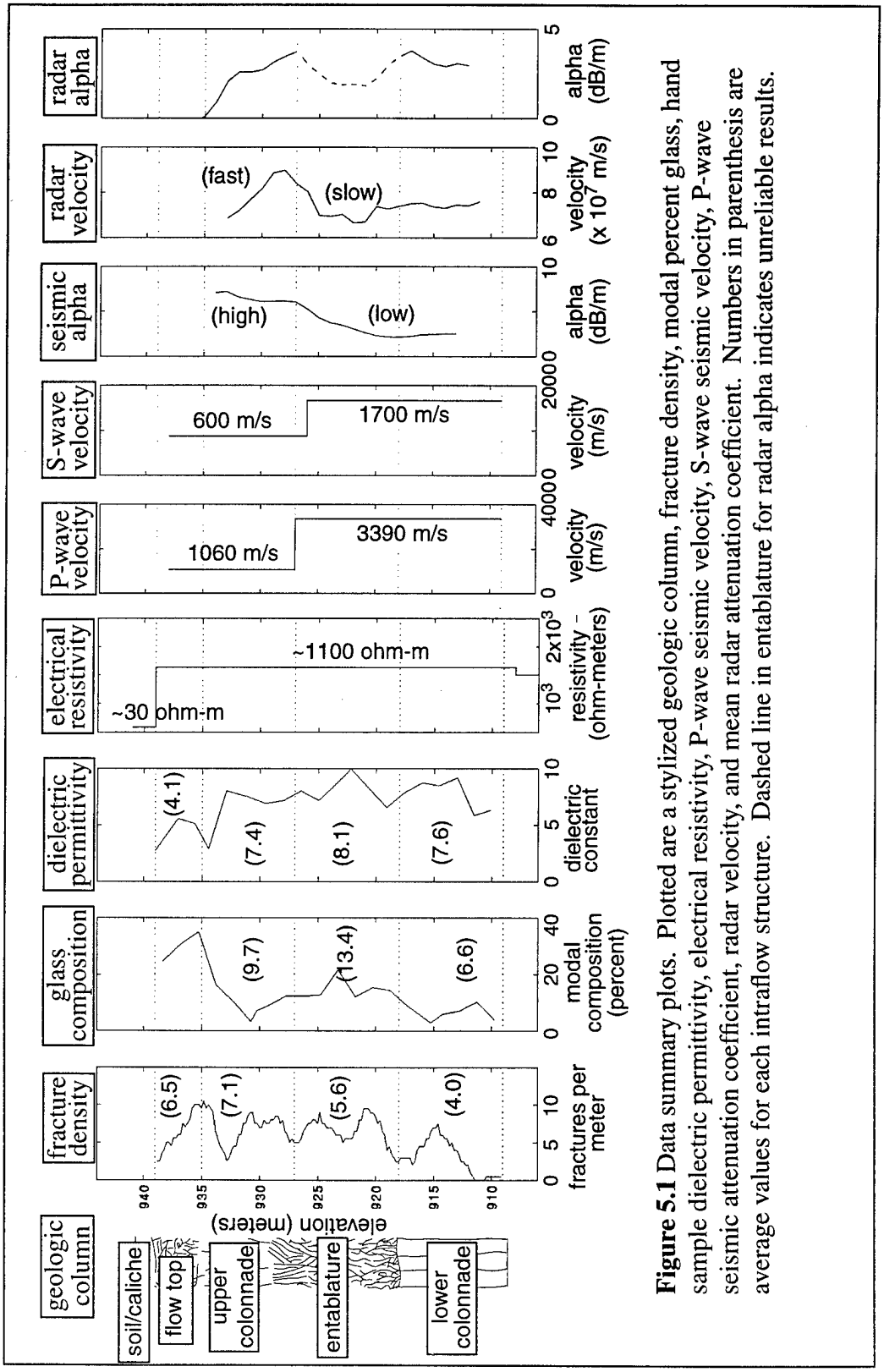

Figure 5.1 Data summary plots. Plotted are a stylized geologic column, fracture density, modal percent glass, hand sample dielectric permittivity, electrical resistivity, P-wave seismic velocity, S-wave seismic velocity, P-wave seismic attenuation coefficient, radar velocity, and mean radar attenuation coefficient. Numbers in parenthesis are average values for each intraflow structure. Dashed line in entablature for radar alpha indicates unreliable results.

- P-wave seismic attenuation is greatest in the upper colonnade, moderate in the entablature, and lowest in the lower colonnade;
- radar velocity is greatest in the upper colonnade and lowest in the entablature, radar velocity in the lower colonnade is nearly equal to the velocity in the upper colonnade;
- radar attenuation is greatest in the entablature (despite calculated results considered unreliable), radar attenuation is nearly the same in the upper- and lower-colonnade.

5.2 Discussion and Conclusions

Inspection of Figure 5.1 shows that some methods were more effective at distinguishing changes in intraflow structures than other methods. Fracture counts showed wide variability throughout the flow, however, sections of core with very low fracture density are seen in the upper colonnade (~933 m elevation) and lower colonnade (~912 m elevation) where expected. Fracture variability throughout the flow is contrary to expectation based on visible examination of outcrop, but confirms the findings of previous researchers. The very subtle shift to lower fractures in the lower colonnade is also consistent with Type III flows. It is possible that the biased sampling of a single vertical borehole does not adequately represent the true nature of fractures in the subsurface, the findings of previous researchers discounts the significance of this in the relationship between borehole and outcrop fracture counts (cf. Meints, 1986).

Modal proportion of glass in the flow follows the expected trends (Long and Wood, 1986), being lower in the colonnades and higher in the entablature. Glass composition is

greatest at the very top of the flow which reasonably cooled quickest after emplacement. An interesting speculation on glass composition and entablature formation is the fate of the water which "quenched" this part of the basalt flow. Although no test were done to measure water content, it is likely that the entablature has a higher proportion of water in the groundmass than the colonnades. This water is unlikely to be free to polarize in an electromagnetic field, and thus directly affect radar wave propagation, however, its presence may be part of the mechanism that causes the difference in the radar propagation between the entablature and other intraflow structures.

Hand sample dielectric constant measurements varied widely within single hand samples. The plot of the mean values of dielectric constant in Figure 5.1 do not show much correlation with intraflow structure, other than extremely low values at the flow top consistent with increased vesicularity here. Since dielectric permittivity is the major factor in radar wave propagation in low conductivity geologic materials, more and better measurements of it on the hand samples is certainly recommended for future work. Correlation of dielectric constants with glass content might also show interesting relationships.

Surface measurements of electrical resistivity of the subsurface could not be measured with sufficient resolution to distinguish intraflow structure, though it clearly shows the contact between surface sediments and the basalt flow. This lack of resolution does not allow for determining if the resistivity is constant in the basalt, or whether there are changes in resistivity which are not measurable. Particular conditions at this site. Because of resistivity's (or, conductivity's) contribution to radar wave propagation, good

measurements of it are also recommended for future research. Electromagnetic induction measurements with a borehole tool may provide the resolution necessary to determine whether or not resistivity (conductivity) changes significantly within the flow. Measurements of resistivity on hand samples would also provide correlation with bulk resistivity values, giving insight into the effect of fractures and infilling materials in the subsurface.

In Figure 5.1, it is seen that P- and S-wave seismic velocities increase significantly below the entablature-upper colonnade boundary. In addition, the seismic P-wave attenuation coefficient decreased below this boundary. The correlation of increased seismic velocity with decreased attenuation is consistent with expectations. Interestingly, the overall average fracture density seen in BH1 core decreases in the entablature compared to the upper colonnade. Thus, there is higher velocity and less attenuation in the zone of fewer fractures (entablature and lower colonnade), and lower velocity and greater attenuation in the zone of higher fractures (upper colonnade). It is possible that changes in seismic velocity and attenuation at the upper colonnade-entablature boundary are the result of increased weathering at the top of the flow, which would decrease seismic velocity and increase attenuation. Fracture aperture may also be affecting seismic velocity. Although the basalt of Lucky Peak is not buried by other formations in any significant way, the fractures at the bottom of the flow may still have more narrow openings than fractures at the top of the flow, thus increasing velocity and decreasing attenuation at the bottom.

Radar wave velocity shows variability through the flow, the fastest velocities are in the upper colonnade and the slowest in the entablature. The calculated radar velocities correspond well with qualitative observations of velocity evident by arrival times in the data records. Radar attenuation, represented by mean α, shows changes between intraflow boundaries. The entablature has the lowest calculated mean α value, which implies lower radar wave attenuation compared to the upper or lower colonnade. However, this result is considered misleading based on visual inspection of the data records. Signal to noise is clearly lower in the entablature compared to the upper- and lower-colonnade (Figure 4.4), and spectral amplitudes show a near complete loss of frequencies above ~50 MHz in the entablature (Figure 4.9). The greater loss of high frequencies and lower signal to noise ratio in the entablature compared to the upper and lower colonnade suggest real differences in attenuation between these intraflow structures that are not indicated by the mean α values calculated with the spectral ratio method. The calculated lower attenuation in the entablature is probably the result of the comparing ratios of noise in the data. Based on visual inspection of the data records and amplitude spectra, it is concluded that attenuation of radar waves is greatest in the entablature.

Measured radar velocities within the basalt are very near or equal to the predicted velocity based on hand sample measurements of dielectric permittivity, bulk measurement of conductivity, and estimate of magnetic permeability. Measured attenuation, as described by α, do not agree with predicted values. That velocity and attenuation do change between the intraflow units suggests that one or more of the constitutive parameters (permittivity, permeability, conductivity) change in the bulk formation in these

intraflow structures. The changes in the "bulk parameters" may be a function of changes inherent in the basalt such as crystal grain size, glass, or water in the groundmass; or, they may be a function of changes in fracture characteristics such as number, aperture, and/or infilling materials (e.g., clays or water). Low resolution of bulk electrical resistivity, and no measurement of bulk magnetic permeability and dielectric permittivity do not allow for clear separation of these effects on the measured changes in radar velocities and attenuations.

6. REFERENCES

ABEM Geoscience, 1990, RAMAC Borehole Radar Manual version 6.4, Mala, Sweden, 60 p.

CRC, 1989, Practical handbook of physical properties of rocks and minerals, R. S. Carmichael, editor, CRC Press, Boca Raton, USA, 552 p.

Degraff, J. M., P. E. Long, and A. Aydin, 1989, Use of joint growth directions and rock textures to infer thermal regimes during solidification of basaltic lava flows, Journal of Volcanology and Geothermal Research, v. 38, p. 309-324

Dougherty, M. E., D. L. Barker, T. R. Wood, and C. F. Knutson, 1995, An evaluation of borehole and ground penetrating radar for vadose zone characterization in fractured basalts, in Proceedings of MGLS Sixth International Symposium on Borehole Geophysics, October, 1995, 17 p.

Dyck, A. V., and R. P. Young, 1985, Physical characterization of rock masses using borehole methods, Geophysics, v. 50, no. 12, p. 2530-2541.

Hansen, W., W. R. Sill, and S. H. Ward, 1973, The dielectric properties of selected basalts, *Geophysics*, v. 38, no. 1, p. 135-139.

Howard, K. A., J. W. Shervais, and E. H. McKee, 1982, Canyon-filling lavas and lava dams on the Boise River, Idaho, and their significance for evaluating downcutting during the last two million years, in B. Bonnichsen and R. M. Breckenridge, eds, Cenozoic geology of Idaho, Idaho Bureau of Mines and Geology Bulletin 26, p. 629-641.

Interpex, 1996, TEMIX XL (TM) user's manual, volume 1 and 2, transient electromagnetic field interpretation software, Interpex Limited, Golden, Colorado.

Keller, G. V., 1987, Rock and mineral properties, in M. N. Nabighian, ed, Electromagnetic methods in applied geophysics, volume 1-theory, (Investigations in geophysics no. 3), Society of Exploration Geophysicists, Tulsa, OK.

Kudo, K. and E. Shima, 1970, Attenuation of shear waves in soil, Bulletin of the Earthquake Research Institute, v. 48, p. 145-158.

Lindberg, J. W., 1989, A numerical study of cooling joint width and secondary mineral infilling in four Grande Ronde Basalt flows of the central Columbia Plateau, Washington, in S. P. Reidel, and P. R. Hooper, eds, Volcanism and tectonism in the

Columbia River flood-basalt province, Geological Society of America, Special Paper 239.

Long, P. E., 1978, Characterization and recognition of intraflow structures, Grande Ronde basalt, RHO-BWI-LD-10, Rockwell Hanford Operations, Richland, Washington.

Long, P. E., M. G. Snow, and N. J. Davidson, 1980, Relationships between internal structures and petrographic textures of basalt flows: Examples from a continental flood tholeiite province [abs], EOS (American Geophysical Union Transactions), v. 61, p 1141; also RHO-BWI-SA-67, Rockwell Hanford Operations, Richland, Washington.

Long, P. E., and N. J. Davidson, 1981, Lithology of the Grande Ronde Basalt with emphasis on the Umtanum and McCoy Canyon flows, in C. W. Myers, and S. M. Price, eds., Subsurface geology of the Cold Creek syncline, RHO-BWI-ST-14, Rockwell Hanford Operations, Richland, Washington, July 1981, 240 p.

Long, P. E., and B. J. Wood, 1986, Structures, textures, and cooling histories of Columbia River Basalt flows, *Geological Society of America Bulletin*, v. 97, p. 1144-1155.

Mabey, D. R., 1982, Geophysics and tectonics of the Snake River Plain, Idaho, in Cenozoic Geology of Idaho, B. Bonnichsen and R. M. Breckenridge, eds, Idaho Bureau of Mines and Geology Bulletin 26, p. 139-153.

McNeill, 1990, Use of electromagnetic methods for groundwater studies, in Ward, S. H., ed., Geotechnical and environmental geophysics, Society of Exploration Geophysicists, Tulsa, OK.

Meints, J. P., 1986, Statistical characterization of fractures in the Museum and Rocky Coulee flows of the Grande Ronde formation, Columbia River basalts, Master's Thesis, Washington State University, 127 p.

Miller, R. D., and D. W. Steeples, 1990, A shallow seismic reflection survey in basalts of the Snake River Plain, Idaho, *Geophysics*, v. 55, n. 6, p. 761-768.

Myers, C. W., and S. M. Price, 1979, Geologic studies of the Columbia River plateau, a status report, RHO-BWI-ST-4, Rockwell Hanford Operations, Richland, Washington.

Olhoeft, G. R., 1990, Tutorial: High frequency electrical properties, U. S. Geological Survey Open File Report 90-0414.

Othberg, K. L., 1994, Geology and geomorphology of the Boise Valley and adjoining

areas, eastern Snake River Plain, Idaho, Idaho Geological Survey, Bulletin 29, 54 p.

Othberg, K. L., and W. L. Burnham, 1990, Geologic map of the Lucky Peak quadrangle, Ada County, Idaho, Idaho Geological Survey Technical Report 90-4, scale 1:24,000

Spry, A., 1962, The origin of columnar jointing, particularly in basalt flows, Geologic Society of Australia Journal, v. 8, no. 2, p. 191-216.

Swanson, D. A., 1967, Yakima basalt of the Tieton River area, south central Washington, Geological Society of America, v. 78, p. 1077-1110.

Telford, W. M., L.P. Geldart, and R.E. Sheriff, 1990, *Applied Geophysics*, second edition, Cambridge University Press, Cambridge, 770 p.

Tomkeieff, S. I., 1940, The basalt lavas of the Giants Causeway district of northern Ireland, Bulletin of Volcanology, ser. 11, v. 6, p. 89-143.

Touloukian, Y. S., W. R. Judd, R. F. Roy, 1989, *Physical Properties of Rocks and Minerals*, volume II-2, Cindas Data Series on Material Properties, Y. S. Touloukian and C.Y. Ho, editors, Hemisphere Publishing Corporation, New York, 548 p.

Turner, G., and A. F. Siggins, 1994, Constant Q attenuation of subsurface radar pulses, Geophysics, v 59, no. 8, p. 1192-1200.

U. S. Army Corps of Engineers, 1948, Preliminary definite project report on Lucky Peak Dam, Boise River, Idaho, Corps of Engineers, Office of the District Engineer, Portland, Oregon, 9 p. plus plates.

U. S. Geological Survey, 1972, Lucky Peak, Idaho, Quadrangle map, 1:24,000 scale.

Ward, S. H., 1967, Electromagnetic theory for geophysical Applications, in Mining Geophysics, edited by D. A. Hansen and others, The Society of Exploration Geophysicists, Tulsa, OK.

Ward, S. H., 1990, Resistivity and induced polarization methods, in S. H. Ward, ed, Geotechnical and environmental geophysics, Society of Exploration Geophysicists, Tulsa, OK.

Whitehead, R. L., 1992, Geohydraulic framework of the Snake River Plain regional aquifer system, Idaho and eastern Oregon, U. S. Geological Survey Professional Paper 1408-B, 32 p.

Whiteman, K. J., J. J. Vaccaro, J. B. Gonthier, and H. H. Bauer, 1994, The hydrogeologic framework and geochemistry of the Columbia Plateau aquifer system, Washington, Oregon, and Idaho, U.S.G.S. Professional Paper 1413-B.

Zohdy, A. A. R. and R. J. Bisdorf, 1989, Programs for the automatic processing and interpretation of Schlumberger sounding curves in Quickbasic 4.0, U. S. Geological Survey Open-File Report 89-137 A&B, 64 p.